TOPICAL REVIEW

An analysis of the dynamical magnetic susceptibility in non-Fermi liquids

N Bernhoeft

CEA-Grenoble, F-38054 Grenoble Cédex, France

Abstract
In recent years there has been growing interest in the existence of strongly correlated, non-Fermi-liquid states with (incipient) phase transitions at zero temperature. A unifying model of the dynamical magnetic susceptibility, $\chi(q, \omega)$, in the non-Fermi-liquid state at a finite temperature above such a quantum critical point is presented which addresses the analysis of both inelastic neutron scattering and thermodynamic experiments on a wide range of materials. The functional forms and symmetries of $\chi(q, \omega)$ derived from these analyses may serve to guide further experimental and theoretical efforts in elucidating the non-Fermi-liquid state, in addition to furnishing the basis for semi-microscopical calculations of thermodynamic and transport properties.

1. Introduction

In recent years there has been growing interest in the existence of strongly correlated, non-Fermi-liquid states with (incipient) phase transitions at zero temperature and the associated quantum critical point (QCP). In particular, attention has been focused on those materials where, at $T = 0$ K, as a function of some control parameter (concentration of defects or impurities, external pressure, magnetic or electric field) the system passes through a continuous phase transition to a new ground state. The QCP occurs at $T = 0$ K; at this temperature, as with normal thermal critical points, one associates a timescale with fluctuations of the system which increases rapidly as the transition is approached; likewise there is a diverging length scale. Real experiments however take place at finite temperature, so, more precisely, we are asking, what are the consequences of the $T = 0$ K transition for physical properties at finite T? In particular we address the question of how to model the dynamical magnetic susceptibility, $\chi(q, \omega)$, dependent on the wavevector, q, and frequency, ω, in the novel non-Fermi-liquid phases which exist in the vicinity of a QCP.

There have been a host of thermodynamic and transport measurements on a wide variety of materials ranging from heavy-fermion metals under conditions of chemical doping or hydrostatic pressure to high-T_c superconductors, all of which exhibit unusual temperature dependencies of, for example, the resistivity, $\rho(T)$, the heat capacity as represented by its linear term, C/T, and the susceptibility, $\chi(T)$. On account of practicalities, there has been little direct experimentation on, for example, the pressure dependence of thermodynamic properties at a fixed and very low temperature [1, 2]. None of this is reviewed here. The regime of reported non-Fermi-liquid behaviour appears to be broad, and even for systems which are far from criticality (e.g. at elevated temperatures) there are possible ways to explain anomalous thermal properties such as non-Fermi-liquid exponents of the resistivity in terms of fluctuations above a QCP.

The dynamical susceptibility holds a central place in the hierarchy of interpretation of experimental data. Lying between microscopic theories based directly on the quantum field and the information derived from scattering, thermodynamic, and transport measurements, it serves as a point of reference for theoretical and experimental workers alike. For this reason, derivation, theoretical or empirical, of its functional form is an important step in building a framework for analysis of a given class of materials. In the following we address primary information available in the published literature, obtained by means of inelastic neutron scattering and thermodynamic probes, on the temperature dependence of $\chi''(q, \omega)$ in strongly correlated paramagnetic materials classified as non-Fermi-liquid systems. A fundamental question is whether the observed non-Fermi-liquid signatures, which include non-exponential relaxation (NER) of the magnetization density and associated logarithmic or power-law divergences of thermodynamic and transport coefficients, arise due to (i) basic non-exponential relaxation processes, (ii) a superposition of relaxation rates arising from sample inhomogeneity and/or the experimental technique, or (iii) an intrinsic, thermodynamic distribution of relaxation rates. Previous fields of inquiry into the non-exponential decay of the structural, dielectric, and magnetic response of supercooled liquids and glass like and crystalline phases in the vicinity of their critical points are well documented [3–7] and, together with recent analyses focused on the non-Fermi-liquid state [8–13], address the three possible mechanisms. In the particular case of the itinerant non-Fermi liquid, it appears that a phenomenology based on (i), as for example, in the marginal Fermi liquid [8], involves sacrificing the basic fermion quasiparticle, a price avoided in alternatives (ii) and (iii). However, aside from preserving the common Fermiology, these latter works differ substantially from the present approach which initiates a new point of view based on the self-consistent

renormalization of the local dynamic susceptibility. The framework which underpins the interpretation of both kinetic and thermodynamic properties is most succinctly summarized by the following *ansatz*. At each wavevector, q, $\chi(\omega)$ is to be formed as the incoherent sum over a *distribution* of relaxation rates, $D(\Gamma)$, of the susceptibilities, $\chi(\Gamma; \omega)$, for the relaxational dispersion of magnetization-density fluctuations with a characteristic rate Γ:

$$\chi(\omega) = \int d\Gamma \, D(\Gamma)\chi(\Gamma; \omega) \tag{1.1}$$

where the explicit q-index on both χ and Γ is suppressed for notational convenience[1]. In the case of a single-exponential decay (SED) rate, for example for a normal Fermi liquid, the distribution, $D(\Gamma)$, is tightly clustered about a central value and nothing is gained from the more general form given above; in contrast, it is precisely the width of the distribution $D(\Gamma)$ that characterizes the NER of the non-Fermi-liquid state. Further, the evolution of $D(\Gamma)$ with temperature, pressure, or doping enables one to map the experimental trajectory through the non-Fermi-liquid phase.

It will be shown in the following sections that equation (1.1) yields a comprehensive analysis of both neutron scattering and thermodynamic data on a series of compounds classified as lying in the non-Fermi-liquid regime. The key (logarithmic) low-temperature divergences in thermodynamic properties realized on approach to the QCP and a full account of the microscopic inelastic neutron scattering data are obtained with one, fixed, flat compact (top-hat) distribution for $D(\Gamma)$ for which the lower and upper limits, Γ_1 and Γ_2, scale as the temperature and are temperature independent respectively. The analytical forms giving this economic description of the diffusive fluctuation spectra in non-Fermi liquids are laid out in section 2. To obtain an overview, the practical relevance of this approach may be assessed by passing directly to the analysis of microscopic and thermodynamic experimental data, including previous scaling studies of $\chi(\omega)$, in section 3.

Aside from its simplicity, one fruitful aspect of the analysis given may be its stimulus in the discussion of the nature of the non-Fermi-liquid state. Amassed evidence points to the spontaneous formation of dynamical heterogeneities and the critical inference of independent fluctuations within which the susceptibility is locally renormalized gives both the form of equation (1.1) and the distribution[2] $D(\Gamma)$. The degree of renormalization, reflecting an exquisite sensitivity of the primary response function to its local environment, may be seen as the defining feature of the non-Fermi-liquid state. The dynamical heterogeneities which drive local renormalizations of the response function may arise in both the primary (magnetization-) density and secondary fields—examples of the latter being fluctuations in local lattice density, orbital current, and crystalline electric field, which couple to the susceptibility via magnetoelastic and spin–orbit terms. Further experiments and the extension of equation (1.1) to encompass the response of finite-frequency oscillators under a distribution of damping rates are discussed in the concluding section and appendix 3.

---

[1] In an alternative viewpoint, if one had sensitive probes and data available, one could imagine a characterization in terms of the current and charge density and higher-order quadrupole, octopole, etc, response functions. However, in general the magnetization-density fluctuations are anticipated to be amongst the lowest-lying excitations and the neutron probe couples in a direct and essentially non-perturbative manner with appropriate (q, ω) resolution and ranges, making the study of magnetization-density fluctuations an obvious choice. In the notation $\chi(a; b)$ the set $\{a\}$ are the parameters and $\{b\}$ the control variables appropriate to the discussion, and the term 'relaxation rate' is used in the conventional shorthand notation to encompass both growth and decay of dynamic processes.

[2] It would be hard to justify the recurrent flat compact form of $D(\Gamma)$ and the simple temperature dependencies of $\Gamma_{1,2}$ found in the analyses of materials with widely different metallurgical properties for a random-defect model.

2. Dynamical susceptibility and thermodynamic properties of non-Fermi liquids

2.1. Model analytical form of $\chi(q, \omega)$

As stated, in the non-Fermi-liquid regime we find $D(\Gamma)$ to show a flat compact distribution with bounding relaxation rates, Γ_1 and Γ_2. This form is motivated within a dynamical heterogeneity model in the following section. It will be seen in section 3 that the constant amplitude of $D(\Gamma)$, representing the equal contribution of relaxation rates, Γ, in conjunction with $\chi(\Gamma)$ based on the standard paramagnon expression, gives at the same time a straightforward interpretation of the neutron spectra and also, in the appropriate limits, the characteristic non-Fermi-liquid divergences in the temperature dependencies of thermodynamic quantities such as θ_1, the NMR lifetime, χ, and C/T.

For SED the spectrum of magnetic fluctuations of the diffusion rate $\Gamma(q)$ is expressed by the susceptibility:

$$\chi(\Gamma; q, \omega) = \frac{\chi(q)\Gamma(q)}{\Gamma(q) - i\omega} \tag{2.1}$$

where Γ depends on microscopic variables which determine the characteristic energy scale a_Γ and wavevector Q_Γ of the fluctuations. In particular, Γ is expected to soften in the vicinity of the wavevector of incipient order, which itself may be temperature dependent. Suppressing parameters, the relaxation rate may be written as $\Gamma(q) = g(q)\chi_0(q)/\chi(q)$ where $g(q)$ is a bare relaxation rate which is renormalized by the magnetic interactions through χ. This follows the general philosophy of the Ginzburg–Landau treatment of classical phase transitions, where one uses χ to express the influence of environmental factors (temperature, pressure, etc) on the relaxation rate. Within a simple Fermi-liquid picture, the product $g(q)\chi_0(q) = u(q)$ is associated with microscopic quantities and unrenormalized by spin- and momentum-conserving interactions; the empirical analysis of section 3 shows that this stability may carry over into the non-Fermi-liquid state. Writing $\Gamma(q) = u(q)\chi^{-1}(q)$, the non-Fermi-liquid generalization of equation (2.1) is given following equation (1.1) as

$$\chi(\omega) = \int d\Gamma \, D(\Gamma) \left[\frac{u}{\Gamma - i\omega} \right]. \tag{2.2}$$

On integration, one obtains, *for each wavevector*, the central model form for the dynamical susceptibility:

$$\chi(\omega) = \frac{u}{\Gamma_2 - \Gamma_1} \ln \left[\frac{\Gamma_2 - i\omega}{\Gamma_1 - i\omega} \right] \tag{2.3}$$

giving an absorptive part:

$$\chi'' = \frac{u}{\Gamma_2 - \Gamma_1} \left[\arctan\left(\frac{\omega}{\Gamma_1} \right) - \arctan\left(\frac{\omega}{\Gamma_2} \right) \right]. \tag{2.4}$$

The generic behaviour of $\chi''(\omega)$ is given in figure 1(a) on linear scales and figure 1(b) with logarithmic axes. From the functional form one sees that the lower bound, Γ_1, acts as the 'roll-up' energy of the response whilst the higher bound, Γ_2, gives the 'roll-off' energy. The peak in the response or mode frequency is at $\sqrt{(\Gamma_1\Gamma_2)}$ which enables, for Γ_2 not too far removed from Γ_1, an approximate description to be given in terms of SED (in the conventional paramagnon form) with a relaxation rate $\Gamma_{\text{para}} = \sqrt{(\Gamma_1\Gamma_2)}$. Examples of the characteristic temperature dependence of the mode frequency, Γ_{para}, as a function of temperature are given in figure 2 where, starting with the uppermost frames (figures 2(a$_1$) and 2(a$_2$)) the distribution $D(\Gamma)$ has been replaced by the simple paramagnetic Curie limit $D(\Gamma) \rightarrow \delta(\Gamma - \Gamma_0)$ with $\Gamma_0 \sim k_B T$.
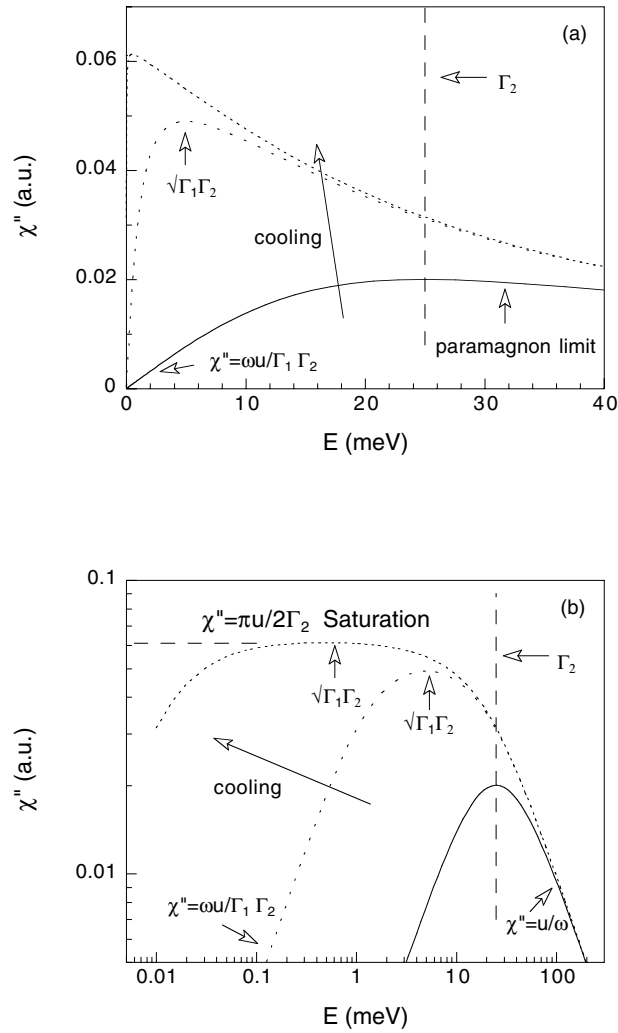
Figure 1. (a) Generic behaviour of a model $\chi''(q, \omega)$ function plotted with linear scales for the non-Fermi liquid, $\Gamma_1 \ll \Gamma_2$, up to the paramagnon limit, $\Gamma_1 = \Gamma_2$. In all curves the high-energy tails are the same. The mode frequency of $\chi''(q, \omega)$ is at $\sqrt{(\Gamma_1\Gamma_2)}$ and can be thought of as the typical energy scale of a fluctuation when Γ_1 is not too far removed from Γ_2. In the strongly non-Fermi-liquid regime there is no typical fluctuation energy; the distribution across frequencies is central to the non-Fermi-liquid response. In the simulations the parameter values for Γ_1, Γ_2 are: 25, 25 meV (paramagnon); 1, 25 meV; and 0.01, 25 meV represented by the solid line; line with spaced points; and line with close points respectively. (b) Generic behaviour of a model $\chi''(q, \omega)$ function plotted with logarithmic scales. Curves of $\chi''(q, \omega)$ with decreasing lower relaxation rate, Γ_1, illustrate the evolution from the paramagnetic limit to the strongly non-Fermi-liquid state. The turning points, $\chi''(q, \omega) = \sqrt{(\Gamma_1\Gamma_2)}$, and high-frequency, $\chi'' = u/\omega$, low-frequency, $\chi'' = u\omega/\Gamma_1\Gamma_2$, and saturation, $\chi'' = \pi u/2\Gamma_2$, regimes are marked. The coding of the Γ_1 values is as in the upper frame.

The same limiting form of $D(\Gamma)$, with the appropriate Curie–Weiss-type $\Gamma(T)$, has previously been applied successfully in the interpretation of the diffusive branch of Fermi-liquid excitations in the paramagnetic phase of 3d transition metal compounds [14–16] and itinerant
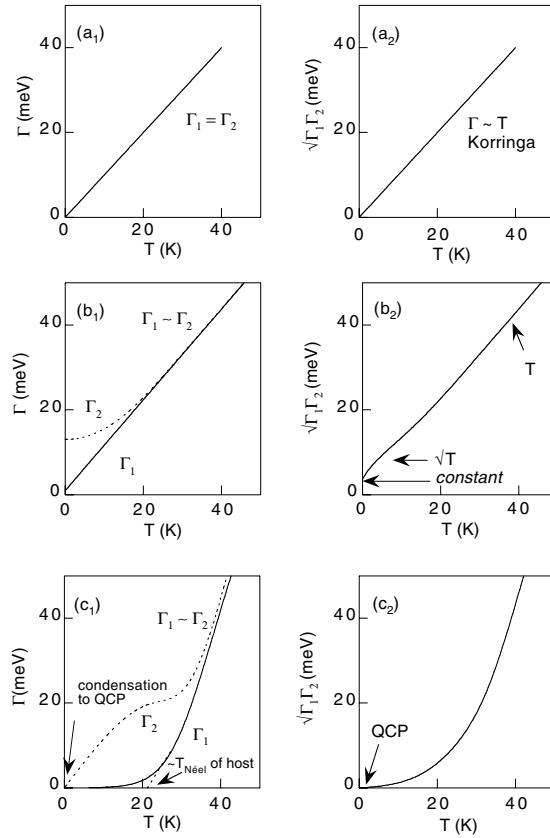
Figure 2. Examples of the relation between Γ_1, Γ_2 and the mode frequency $\Gamma_{para} = \sqrt{(\Gamma_1 \Gamma_2)}$. In the top frames $((a_1)$ and $(a_2))$ the case of an uncorrelated paramagnet is given (Korringa relaxation). In (b_1) the upper bound of the distribution, Γ_2, is taken to increase from a constant at low temperature giving rise to characteristic $\sqrt{T}$ dependence of the mode relaxation rate as found in some non-magnetically ordering, heavy-fermion materials, a behaviour which has previously been derived for the relaxation of a Kondo lattice [20]. At the lowest temperatures, if Γ_1 saturates, the $\sqrt{T}$ rise is replaced by a constant value as in the single-ion Kondo model [12]. The overall low-temperature behaviour is similar to that observed for UCu$_5$ [22]. In frame (c_1) the faster than Korringa rates may reflect extra relaxation channels (e.g. phonon-assisted decorrelation in the presence of magnetostrictive or spin–orbit coupling) or arise on account of local saturation of the susceptibility. The soft lower limit, Γ_1, indicates slow relaxation rates due to the build-up of magnetic correlations at low temperature with, eventually, a merging of relaxation rates and condensation towards a QCP.

antiferromagnets [17–19]. On entering the non-Fermi-liquid state, frames (b_1), and (b_2), the degeneracy of the relaxation rates is lifted at low temperature. Given that the relaxation time scales with the susceptibility, close to a QCP in q and T we anticipate $\Gamma_1 \sim a_1 k_B (T - T_1)$ where $T_1 \sim 0$ (solid line in frame (b_1)). The upper limit, Γ_2, reflecting the shorter lifetime of heterogeneities with suppressed susceptibility, takes the form $\Gamma_2 \sim a_2 k_B (T - T_2) + b q_2^2 + \cdots$ where T_2 is negative and significant (compared with T) and q_2 is the distance in momentum space from the soft wavevector, Q_2 (which is not necessarily the same as that of Γ_1). When $T_{1,2} \leqslant 0$, as illustrated here (i.e. no ordering), and at temperatures such that $T < |T_{1,2}|$, the paramagnon approximation yields $\Gamma_{para} \sim$ constant (finite intercept on the ordinate in frame (b_2)). At intermediate temperature where $|T_1| < T < |T_2|$ the variation is $\sim\sqrt{T}$,
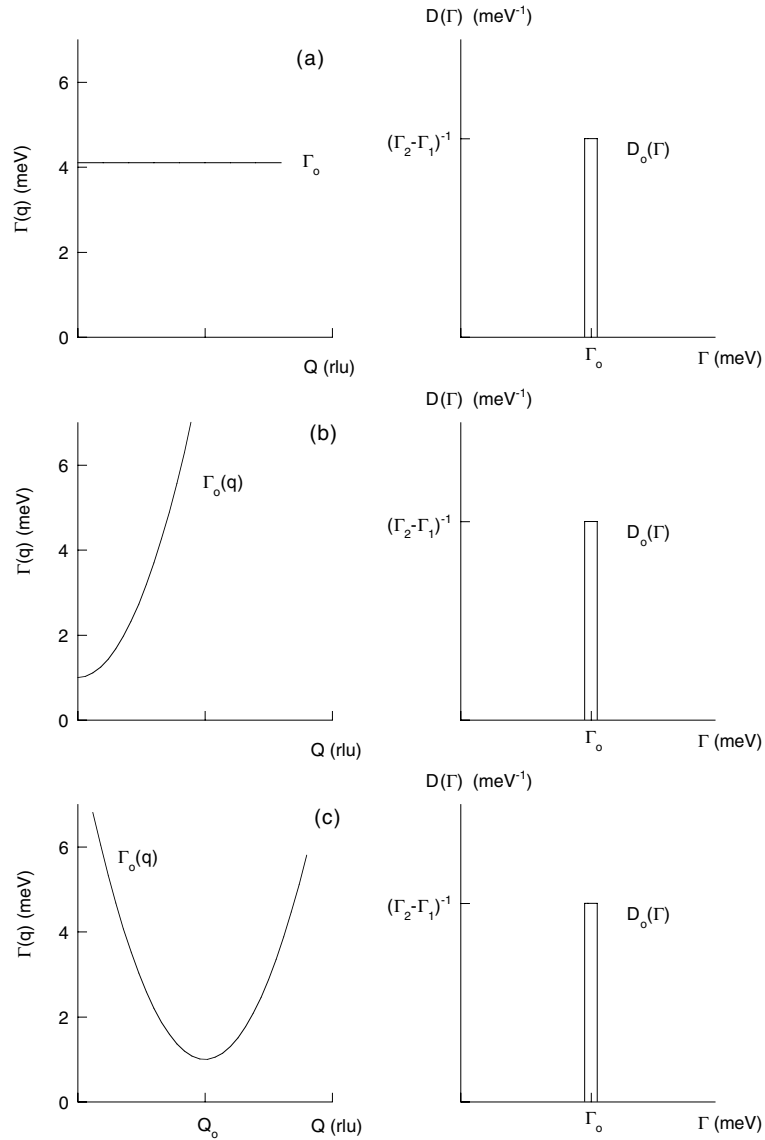
Figure 3. Representations of the relaxation rates and distribution functions, $D_0(\Gamma)$, in type 1 non-Fermi liquids. Real-space averaging or reciprocal-space smearing generates an effective distribution $D(\Gamma)$. Spatial averaging is significant when the relaxation rate depends strongly on inhomogeneities in the distribution of chemical or external fields. Smearing arises both from dispersion and anisotropy in the relaxation rate and the explicit or implicit averaging taking place in the experiment. For example in neutron scattering experiments it is the q-space resolution employed; in NMR it arises from the local and incoherent nature of the probe. In (a) the illustrated response is locally, in (b) ferromagnetically, and in (c) antiferromagnetically biased.

and at sufficiently high temperatures when $\Gamma_1 \sim \Gamma_2 \sim T$ there is a return to SED and the generalized Korringa form, $\Gamma \sim ak_B T$. Similar temperature dependencies for Γ_{para} have previously been derived in models of the Kondo state [12, 20] and observed in some non-ordering heavy-fermion materials [21, 22] which, interestingly, over intermediate-temperature intervals
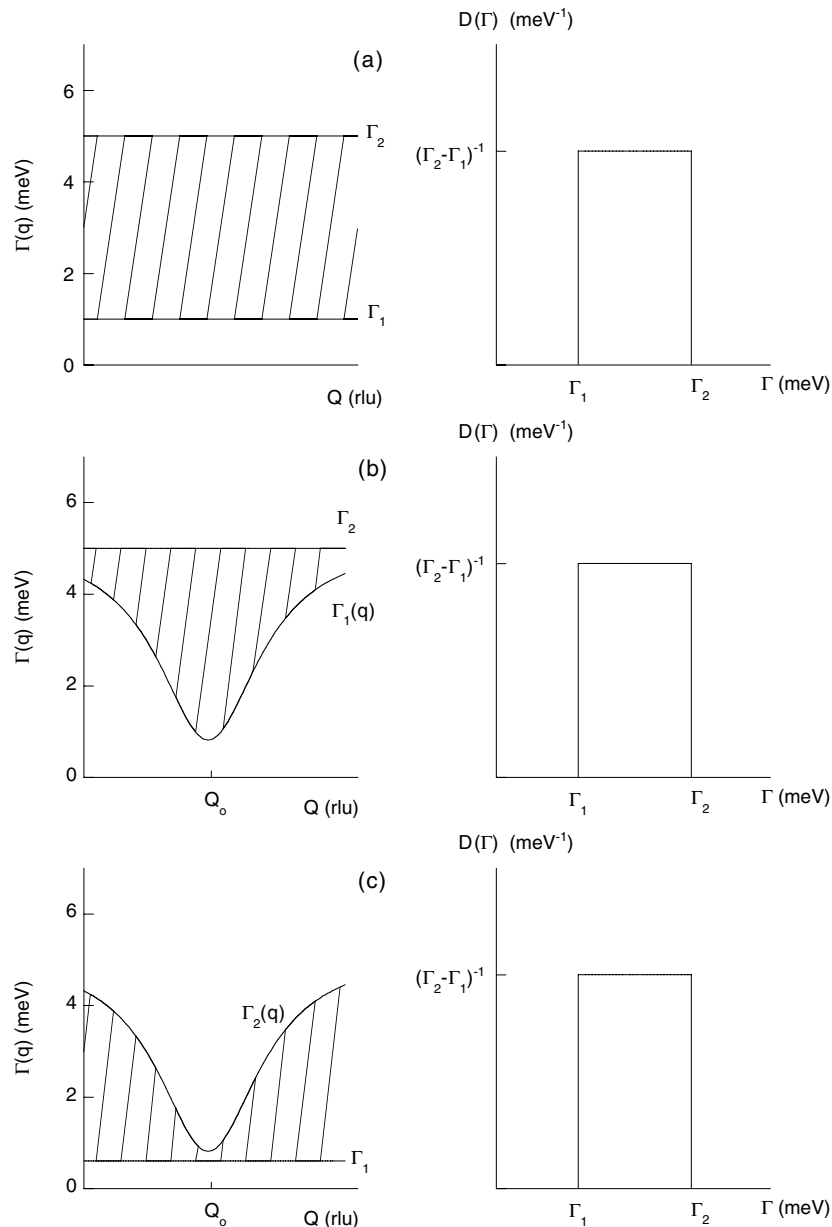
Figure 4. Representations of the relaxation rates and distribution function, $D(\Gamma)$, in type 2 non-Fermi liquids. In (a) a local intrinsic distribution of relaxation rates is illustrated. In (b) there is one soft relaxation wavevector, whilst in (c) the lower bound of all wavevectors is low. Such materials would exhibit markedly different thermodynamic properties (C/T, χ, etc). The distributions may depend on the composition and external environment.

exhibit an anomalous evolution of $\rho(T)$ [23]. In frame (c_1), for a material driven from an (antiferro-) magnetic ground state by doping, pressure, etc, the (wavevector dependent) susceptibility may be enhanced in the presence of residual magnetic correlations yielding, from an initial Curie–Weiss form of Γ_1 at high temperature, a suppression below the Korringa rate

for[3] $T < T_{\text{Néel host}}$. The upper relaxation rate may keep the form illustrated in frame (b_1) or, if on approaching the lowest temperatures a QCP intervenes, it will fall concomitantly with Γ_1.

2.2. Inferential models for $D(\Gamma)$

Expanding upon equation (1.1), the experimentally determined susceptibility is expressed as

$$\chi_{\text{expt}}(q, \omega) = \left\langle \{\chi(q, \omega)\}_{t_{\text{probe}}, v_{\text{probe}}} \right\rangle_{T_{\text{expt}}, V_{\text{expt}}} \tag{2.5}$$

where $\langle\ \rangle_{T_{\text{expt}}, V_{\text{expt}}}$ represents the incoherent sum over the experimental time and volume of the set $\{\chi(q, \omega)\}$ of susceptibilities determined over the probe coherence time and volume (appendix 1). The respective restrictions of implicit ensemble and space-time averaging limit details in the empirical information concerning $D(\Gamma)$; however, to orient the discussion it is nevertheless useful to invoke inferential, microscopic images for $D(\Gamma)$.

First we distinguish type 1 and type 2 distributions. NER from type 1 distributions arises from spatial, time-independent averages over the experimental volume of sharp distributions $D_0(\Gamma) = \delta(\Gamma - \Gamma_0)$ with different values of Γ_0. The sources of which may be extrinsic—for example, gradients in temperature or applied pressure—or intrinsic entropy-driven chemical disorder or microstructural defects. The fluctuations may be (a) local or correlated in momentum space, (b) ferromagnetic, or (c) antiferromagnetic as sketched in figure 3. In a similar manner, both implicit and explicit q-space averaging of a dispersive and/or anisotropic response within V_{expt}, as for example in NMR, heat capacity, or neutron scattering characterizations, may yield non-Fermi-liquid like signatures via a type 1 distribution. In general, both spatial inhomogeneity (i.e. sample contribution) and q-space averaging (i.e. probe contribution) contribute to the final effective distribution $D(\Gamma)$ in a given experiment.

In contrast, type 2 NER and hence non-Fermi-liquid behaviour arises from an intrinsic distribution of relaxation rates, i.e. is independent of the above averaging. Wavevector independent relaxation rates give a local non-Fermi-liquid (figure 4(a)); preferential mode softening yields a non-Fermi liquid with spatial correlations (figures 4(b), 4(c)). Within given limits of observation, fluctuations arising from a figure 4(b) distribution may be interpreted as a quasi-q-independent (localized) high-frequency response together with a soft q-dependent (correlated) response; an example may be $Ce_{1-x}La_xRu_2Si_2$ [24]. The distribution of figure 4(c) exhibits overall mode softening together with fluctuations focused at Q_0, an example of which is found in $CeCu_{5.9}Au_{0.1}$ [25]. Such materials are expected to exhibit markedly different thermodynamic properties (evolution and values of C/T, χ, etc). Picking up the spatial dependence we recall that the above considerations apply for each value of q and volume of static inhomogeneity (on top of the dynamic heterogeneities), leading to possible type 1 averaging on top of the type 2 non-Fermi-liquid response.

Whilst at present no unambiguous experimental evidence in favour of a given microscopic model for the non-Fermi-liquid phase exists[4], and all empirical analyses devolve to equation (1.1), we stress an interpretation based on internal renormalization of the relaxation

---

[3] Such low relaxation rates over extended regimes in temperature may be anticipated to favour the condensation of novel condensed states.

[4] The phenomenology of Varma *et al* [8] is based on a hypothetical form for $\chi(q, \omega)$ in a homogeneous system for which a novel (marginal Fermi-liquid) one-particle Green's function is derived. The assumed homogeneity and wavevector independence of excitations excludes derivation of $\chi(q, \omega)$ via a distribution of response functions in either real or momentum space. At this level the model suffers from unbounded high-energy excitations which lead to formal divergences of, for example, the static susceptibility. Unfortunate confusion in physical reasoning may arise through the use of similar functional forms for $\chi(q, \omega)$ in the interpretation of a local response or to model experimental data averaged in momentum space. The works of Hayden *et al* [9, 11] and Keimer *et al* [10] are for distributions based on the wavevector averaged or local response of a Fermi-liquid like SED response as discussed in section 3.3.

rate of incoherent, spontaneous fluctuations (dynamical heterogeneities). This model has a general motivation in an anharmonic (mode-coupled) system [4–7] and, since it preserves the underlying form, yields a smooth crossover between the SED (Fermi-liquid) and NER (non-Fermi-liquid) response. To introduce the dynamic model it is considered frozen at one instant, and a convenient starting point is to rewrite equation (2.5) in terms of its Fourier transform as the instantaneous magnetization-density correlation function:

$$C_{T_{\text{expt}}, V_{\text{expt}}} = \left\langle \left\{ \frac{1}{v_{\text{probe}}} \int_{-v_{\text{probe}}/2}^{v_{\text{probe}}/2} \mathrm{d}r' \, m(r', t) m(r + r', t) \right\} \right\rangle. \tag{2.6}$$

Mathematically the integral in equation (2.6) may be broken down as a sum of integrals over intervals v_i lying within a given v_{probe} (cf. figure A2 given in the temporal domain):

$$C(r) = \sum_i g_{ii}(v_i; r) + \frac{1}{2} \sum_{i,j} g_{ij}(v_i; r) \tag{2.7}$$

where, for $v_i < v_{\text{probe}}$ (see appendix 1),

$$g_{ij}(v_i; r) = \frac{1}{v_i} \int_{-v_i/2}^{v_i/2} \mathrm{d}r' \, m_i(r') m_j(r + r'). \tag{2.8}$$

In the case where over all intervals, v_i, the magnetization-density correlations are characterized by the *same* relaxation rate, Γ, nothing is changed and SED is recovered. In modelling the non-Fermi-liquid state, the (physical) generalization that we have in mind is as follows: whilst for a given v_i the response can be characterized by the relaxation rate Γ_i, an adjacent fluctuation may have a different characteristic relaxation rate Γ_j. Taking into account the dynamical nature of the problem demands a parallel consideration in the temporal domain; this and the role of dynamic phase coherence are discussed in appendix 1.

Within this framework a power-law (scale-free) distribution of fluctuating volumes, for both SED and non-Fermi-liquid states, follows on the assumption of incoherence which enables the total energy of fluctuating volumes v_i to be expressed in terms of their degeneracy, n_i, as $E_{v_i}^T = n_i v_i E_{v_i}$. Under set external conditions, given that the energy density, E_{v_i}, is constant, i.e. the thermodynamic condition that $E_{v_i}^T$ is an extensive quantity [4–7, 26], a set of unconstrained, incoherent fluctuations then have equal probabilities. Equating this with their volume representation, $n_i v_i / V_{\text{expt}}$, yields $n_i v_i = $ constant. In the non-Fermi-liquid phase, given an identification of the local renormalization of Γ_i (i.e. χ_i) with volume v_i, the normalized contribution of modes in the interval $\mathrm{d}\Gamma$ about Γ_i is proportional to their volume representation, $D(\Gamma)\,\mathrm{d}\Gamma \leftrightarrow n_i v_i / V_{\text{expt}}$, yielding a flat compact distribution for $D(\Gamma)$.

The distinction between SED and non-Fermi-liquid states thus lies in the distribution of relaxation rates present in the latter. The low-temperature coherent Fermi-liquid state, characteristic of strongly correlated electronic systems, may then be seen in primitive analogy with the different microscopic states realized at discontinuous and continuous transitions of phase. At a discontinuous transition, finite correlation lengths permit the coexistence of multiple phases; in contrast, the diverging length scale of fluctuations forces the system to be in a unique critical state on approach to a continuous phase transition. The divergence of scale, spatial or temporal, is equivalent to the removal of competing phases. In the passage to a QCP the divergence of (v_i, τ_i) accompanies the condensation of a unique relaxation rate out of the non-Fermi-liquid distribution. Thus, whilst the non-Fermi liquid holds the middle ground, SED may be anticipated at both extremes of temperature—that is, both at the very lowest, when the system has selected and condenses in a continuous fashion into one of the

competing ground states[5], and at sufficiently high temperatures, where correlations fall away and the system behaves as a simple paramagnet[6] (cf. figure 2(c)).

2.3. Non-Fermi-liquid parameter

Since the variable T employed in figure 2 can in general be replaced by any convenient tuning parameter, e.g. composition, pressure, or magnetic field, it may be of use in constructing phase diagrams and the selection of materials to have some index of the non-Fermi-liquid state. A suggestive measure is given by the ratio of the width of the distribution $D(\Gamma)$ to the mode frequency of $\chi''(\omega)$; i.e. define a parameter:

$$NFL = (\Gamma_2 - \Gamma_1)/\sqrt{\Gamma_1 \Gamma_2}. \tag{2.9}$$

This ratio, which goes to zero as Γ_1 and Γ_2 tend to a common relaxation rate and diverges as the distribution becomes large, is plotted in figure 5 for the typical cases considered in figure 2.
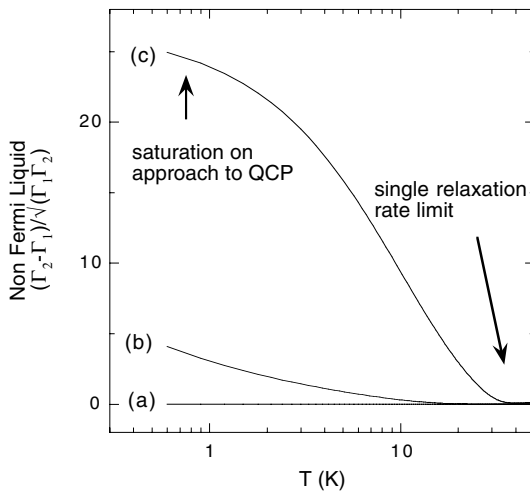

Figure 5. The thermal evolution of the non-Fermi-liquid parameter, equation (2.9), is given for cases (a) to (c) of figure 2.

2.4. Scaling of the dynamical susceptibility with $E/k_B T$

A generalized scaling of the dynamical susceptibility, $\chi'' \propto T^{-\alpha} g(\omega/k_B T)$, which retains T as an explicit parameter has been proposed with, however, very different scaling laws and values of the exponent α invoked to characterize different materials around the antiferromagnetic QCP [9, 13, 25]. The interest lies in going beyond the standard model, which scales in the Curie regime with $\alpha = 1$ in the vicinity of the critical point, and relaxing α to find scaling laws which may yield significant restrictions on proposed theoretical models of the fluctuation spectrum [6, 27]. The freedom given to α (which governs the energy or, equivalently, timescale) is reminiscent of the introduction of an anomalous exponent in the spatial scaling of static critical phenomena at a continuous phase transition. At the critical point the domination of physical properties by fluctuations over a wide distribution of length scales brings in a new spatial parameter (the lower cut-off $\sim$ lattice parameter) in addition to the correlation length (upper cut-off). From the perspective of the dynamical heterogeneity model, a correspondence may

---

[5] With the proviso that the trajectory to this state is not blocked by a transition to a non-Fermi-liquid phase, e.g. a superconducting ground state.

[6] With the proviso that this trajectory is not cut short by a change of state, e.g. structural transformation, melting.

be made with the introduction of a broad, bounded distribution of relaxation rates and the anomalous values assumed by α [7].

To motivate the analysis of $\chi''(\omega)$ using scaling plots, we follow the behaviour of the high- and low-frequency asymptotes of the dynamical susceptibility. The high-energy asymptote of equation (2.4) is

$$\lim_{\omega \to \infty} \left[\ln(\chi'') \right] = -\ln(\omega) + \ln(u) \tag{2.10}$$

i.e. a measure of the bare relaxation rate unrenormalized by local non-Fermi-liquid interactions expressing the physical result that on a sufficiently short timescale the response is not modified by its environment; this asymptote then becomes essentially temperature independent. The low-frequency asymptote

$$\lim_{\omega \to 0} \left[\ln(\chi'') \right] = \ln(\omega) + \ln(u) - \ln(\Gamma_1 \Gamma_2) \tag{2.11}$$

exhibits the full weight of non-Fermi-liquid renormalization with an implicit temperature dependence through both Γ_1 and Γ_2. For the scaled variable, $\omega/k_B T$, the asymptotes behave as follows:

$$\lim_{\omega \to \infty} \left[\ln(\chi'' \{k_B T\}^\alpha) \right] = -\ln(\omega/k_B T) + \ln(u) + (\alpha - 1) \ln(k_B T) \tag{2.12}$$

and

$$\lim_{\omega \to 0} \left[\ln(\chi'' \{k_B T\}^\alpha) \right] = \ln(\omega/k_B T) + \ln(u) + (\alpha + 1) \ln(k_B T) - \ln(\Gamma_1 \Gamma_2) \tag{2.13}$$

giving, for a scaling exponent α close to unity, a temperature-independent behaviour for data lying in the high-frequency (ideal-gas, Curie) limit with a scaling function of asymptotic form: $\lim_{\omega \to \infty} g(\omega/k_B T) = (\omega/k_B T)^{-1}$. Data obtained in the low-frequency limit have an effective scaling exponent which depends critically on the temperature dependence of the relaxation rates $\Gamma_{1,2}$, maintaining its temperature independence for

$$\alpha = \frac{\ln(\Gamma_1 \Gamma_2)}{\ln(k_B T)} - 1 \tag{2.14}$$

with the scaling function $\lim_{\omega \to 0} g(\omega/k_B T) = (\omega/k_B T)$.

To initiate the discussion we consider the approximate scaling which obtains in the paramagnetic, $\Gamma \sim \sqrt{(\Gamma_1 \Gamma_2)}$, Curie–Weiss limit with $u \approx$ constant: $\Gamma \approx a k_B (T - T_0)$. Temperature independence is maintained for the upper asymptote with α close to unity, whilst the low-frequency limit requires

$$\alpha = 2 \frac{\ln(a k_B (T - T_0))}{\ln(k_B T)} - 1. \tag{2.15}$$

In the Korringa regime, where $a \approx 1$ and $T_0 = 0$, exact scaling obtains for both high- and low-frequency limits with exponent $\alpha = 1$. Maintaining the condition $a \approx 1$ and varying T_0 enables one to explore the Curie–Weiss regime where approximate scaling occurs for $\alpha < 1$ with $T_0 < 0$, i.e. no spontaneous magnetic order, and for $\alpha > 1$ when $T_0 > 0$ in the presence of a finite-temperature phase transition. The three cases are illustrated for the dynamical response at 300 K and 120 K with values of $a = 0.97$, $T_0 = 0$ and ± 46 K (4 meV) in figure 6.

Beyond the paramagnetic approximation, to satisfy the high-frequency asymptote the scaling exponent should remain close to unity; and, for materials selected by reason of doping, applied pressure, etc as being subcritical, i.e. showing no finite-temperature transition, on the basis of the above considerations, we may anticipate sublinear scaling. The recurrent observation of $\alpha < 1$ [13, 25] is reinforced in the light of the habitual (low-temperature)

behaviour of the relaxation rates illustrated in figure 2(b_1), $\Gamma_1 \approx a_1 k_B (T - T_1)$ and $\Gamma_2 \approx$ constant, which suggest a value for α compatible with the low-frequency asymptote as follows:

$$\alpha = \frac{\ln(a_1 \Gamma_2)}{\ln(k_B T)} + \frac{\ln(k_B (T - T_1))}{\ln(k_B T)} - 1. \tag{2.16}$$

As tuning of composition and the environment causes $T_1/T \to 0$, i.e., at low temperature, Γ_1 becomes critical, this imposes the condition

$$[k_B T]^\alpha = \text{constant} \tag{2.17}$$

giving temperature independence as $\alpha \to 0$. To optimize the empirical scaling in a given system, the compromise between the low- and high-frequency requirements of the exponent, $0 \leqslant \alpha \leqslant 1$, will depend on the extent and temperature range of the data treated. At a practical level, data sets are rarely sufficiently extensive in frequency to reach both asymptotes and an approximate criterion for the required value of the anomalous exponent to make a compact representation of the data is that $\chi''(\omega)[k_B T]^\alpha$ in the (measured) high-frequency limit at high temperature should overlap with $\chi''(\omega)[k_B T]^\alpha$ in the (measured) low-frequency limit at low temperatures:

$$\chi''(\omega_{\text{high}})[k_B T_{\text{high}}]^\alpha \approx \chi''(\omega_{\text{low}})[k_B T_{\text{low}}]^\alpha. \tag{2.18}$$

These alternative, heuristic, derivations of the scaling exponent which are exploited further in section 3 in no way diminish the usefulness of the concept over given temperature and frequency ranges; however, they do underline the fact that empirical scaling laws and exponents may depend on both the temperature and the part (high or low frequency with respect to $\sqrt{(\Gamma_1 \Gamma_2)}$) and the proportion of the spectrum measured, i.e. the experimental dynamic range.

2.5. Implications for bulk properties

2.5.1. $\chi(T)$.
From equation (2.3) the real part of the susceptibility is given as

$$\chi'(q, \omega) = \frac{u}{2(\Gamma_2 - \Gamma_1)} \ln\left[\frac{\omega^2 + \Gamma_2^2}{\omega^2 + \Gamma_1^2}\right] \tag{2.19}$$

giving for the bulk, $q = 0$, mode, at sufficiently low frequencies,

$$\chi' = \frac{u}{(\Gamma_2 - \Gamma_1)} \ln\left[\frac{\Gamma_2}{\Gamma_1}\right] \tag{2.20a}$$

which, since measurement of χ has no intrinsic energy resolution, may more aptly be expressed in terms of the local renormalized susceptibilities:

$$\chi' = \frac{1}{(\chi_2^{-1} - \chi_1^{-1})} \ln\left[\frac{\chi_2^{-1}}{\chi_1^{-1}}\right]. \tag{2.20b}$$

For the approximate forms $\Gamma_1 = a_1 k_B (T - T_1)$ and $\Gamma_2 = a_2 k_B (T - T_2)$, the characteristic non-Fermi-liquid logarithmic divergence occurs in the low-temperature limit, $(\Gamma_2 - \Gamma_1) \sim$ constant, $\Gamma_2 \sim$ constant, and $\Gamma_1 \sim T$:

$$\chi' = a - b \ln[T] \tag{2.21}$$

whilst χ' saturates for conditions of composition, pressure, field, etc where at sufficiently low temperature $\Gamma_1 \sim$ constant and $\Gamma_2 \sim$ constant. Finally, in the presence of a zero-temperature phase transition, either

$$\chi' \to \frac{A}{(a_2 - a_1)T} \tag{2.22}$$

or, in the case where $\Gamma_1 \approx \Gamma_2$, a return to Fermi-liquid behaviour occurs (equation (2.1)).
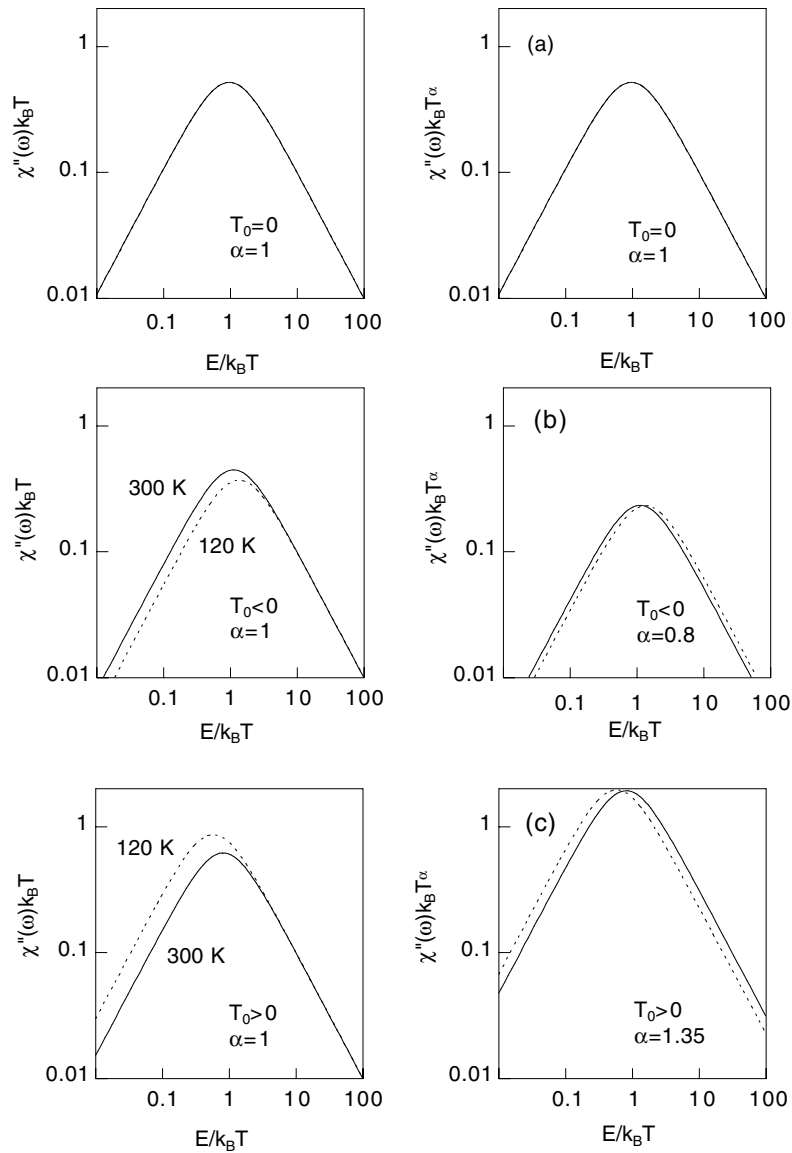
Figure 6. In parts (a) to (c) the linear, sublinear, and hyperlinear scaling plots obtained for the general paramagnetic approximation, $\Gamma \sim \sqrt{(\Gamma_1 \Gamma_2)}$, discussed in section 2.4 are shown. The left/right-hand frames have $\chi'' k_B T$ and $\chi'' k_B T^\alpha$ as ordinate respectively. (a) The solid/dotted curve is drawn for $\sqrt{(\Gamma_1 \Gamma_2)} = 25$ meV ($\Gamma_1 = 24.75$ meV, $\Gamma_2 = 25.25$ meV) at 300 K and for $\sqrt{(\Gamma_1 \Gamma_2)} = 10$ meV ($\Gamma_1 = 9.75$ meV, $\Gamma_2 = 10.25$ meV) at 120 K with a scaling exponent $\alpha = 1$. (b) The solid/dotted curve is drawn for $\sqrt{(\Gamma_1 \Gamma_2)} = 29$ meV ($\Gamma_1 = 28.75$ meV, $\Gamma_2 = 29.25$ meV) at 300 K and $\sqrt{(\Gamma_1 \Gamma_2)} = 14$ meV ($\Gamma_1 = 13.75$ meV, $\Gamma_2 = 14.25$ meV) at 120 K with a scaling exponent $\alpha = 0.8$. (c) The solid/dotted curve is drawn for $\sqrt{(\Gamma_1 \Gamma_2)} = 21$ meV ($\Gamma_1 = 20.75$ meV, $\Gamma_2 = 21.25$ meV) at 300 K and $\sqrt{(\Gamma_1 \Gamma_2)} = 6$ meV ($\Gamma_1 = 5.75$ meV, $\Gamma_2 = 6.25$ meV) at 120 K with a scaling exponent $\alpha = 1.35$.

2.5.2. NMR. Assuming temperature-independent coupling constants, the inverse of the spin–lattice relaxation time, θ_1, is proportional to the low-frequency limit of $T \sum_q \chi''(q, \omega)/\omega$.

Accounting for the local nature of the probe is straightforward for q-independent modes or when the relaxation time is strongly peaked around a critical wavevector, giving

$$\frac{1}{\Theta_1} \approx T\left(\frac{u}{\Gamma_1\Gamma_2}\right). \tag{2.23}$$

In instances where the fluctuations relaxing the nuclear polarization are dominantly $2d$, the sum over q is essentially the same as that used in deriving the ($2d$) correlation function (section A2.2 of appendix 2), giving

$$\frac{1}{\Theta_1} \approx T\frac{\pi\chi}{\lambda^2}\left(\frac{\Gamma_2 - \Gamma_1}{\Gamma_1\Gamma_2}\right) \tag{2.24}$$

for an in-plane magnetic correlation length λ. In the limit $\Gamma_2 \gg \Gamma_1$ (i.e. $\lambda^2 Q_{max}^2 \gg 1$) this gives

$$\frac{1}{\Theta_1} \approx T\frac{\pi\chi}{\lambda^2\Gamma_1}. \tag{2.25}$$

Thus, for compositions where Γ_1 maintains its characteristic form and Γ_2 is large and essentially temperature independent, one obtains for fluctuations that are (i) strongly peaked around a critical wavevector, (ii) focused in a plane with quadratic dispersion, or (iii) have wavevector independent relaxation rates,

$$\frac{1}{\Theta_1} \approx T\left(\frac{1}{T - T_1}\right). \tag{2.26}$$

This yields, in the vicinity of the QCP composition where $T_1 \sim 0$ K, an inverse spin–lattice relaxation time independent of temperature; on passing towards a magnetically ordered composition, T_1 becomes positive, and a characteristic divergence in θ_1^{-1} is observed on cooling from above the critical point. Doping on the other side of the QCP sends T_1 negative and θ_1^{-1} initially grows and then saturates with increasing T.

2.5.3. Entropy and low-temperature heat capacity. For a non-Fermi liquid modelled on the existence of a distribution of independent relaxational modes, the entropy may be developed as a sum over the contributions of a set of overdamped oscillators [7, 26, 28–30]. This allows an estimate to be made of the contribution of such modes to thermodynamic properties, in particular the low-temperature heat capacity [28, 29]:

$$\lim_{T \to 0}\frac{C}{T} = \frac{\upsilon\pi k_B^2}{3}\sum_{\text{modes}}\frac{1}{\Gamma} \tag{2.27}$$

where υ is the polarization index. Considering the non-Fermi-liquid state, the sum over the primary (magnetic) relaxational modes may be given as

$$\lim_{T \to 0}\frac{C}{T} = \frac{\upsilon\pi k_B^2}{3}\sum_{q}\int d\Gamma\,\frac{D(\Gamma)}{\Gamma} \tag{2.28}$$

which, after integration over $D(\Gamma)$, gives

$$\lim_{T \to 0}\frac{C}{T} = \frac{\upsilon\pi k_B^2}{3}\sum_{q}\frac{1}{\Gamma_2 - \Gamma_1}\ln\left[\frac{\Gamma_2}{\Gamma_1}\right]. \tag{2.29}$$

For wavevector independent relaxation rates, Γ, measured in meV, and with η expressing the number of effective (magnetic) degrees of freedom per atom per polarization, summing the

three degenerate polarizations over the Brillouin-zone volume, $(2\pi)^3/$(unit-cell volume), in the paramagnetic state,

$$\lim_{T \to 0} \frac{C}{T} = \eta \frac{2.25}{\Gamma_2 - \Gamma_1} \ln \left[\frac{\Gamma_2}{\Gamma_1} \right] \text{ J mol}^{-1} \text{ K}^{-2} \qquad (2.30)$$

(section A1.6 of appendix 1). For comparison, the corresponding result for local SED is

$$\lim_{T \to 0} \frac{C}{T} = \eta \frac{2.25}{\Gamma_0} \text{ J mol}^{-1} \text{ K}^{-2} \qquad (2.31a)$$

and for dispersive SED of the (homogeneous) Fermi liquid with a linear relaxation rate,

$$\lim_{T \to 0} \frac{C}{T} = \eta \frac{3.38}{\Gamma_{\text{upper}}} \text{ J mol}^{-1} \text{ K}^{-2} \qquad (2.31b)$$

where $\Gamma_{\text{upper}} = \gamma q_{\text{zone bdy}} \chi_{\text{FL}}^{-1}$. Giving the relative non-Fermi-liquid enhancements as

$$\left. \frac{C}{T} \right|_{\text{NFL}} = \left. \frac{C}{T} \right|_{\text{localSED}} \frac{\Gamma_0}{\Gamma_2 - \Gamma_1} \ln \left[\frac{\Gamma_2}{\Gamma_1} \right] \qquad (2.32a)$$

and

$$\left. \frac{C}{T} \right|_{\text{NFL}} = \left. \frac{C}{T} \right|_{\text{FL}} \frac{2}{3} \frac{\Gamma_{\text{upper}}}{\Gamma_2 - \Gamma_1} \ln \left[\frac{\Gamma_2}{\Gamma_1} \right] \qquad (2.32b)$$

respectively. In the presence of dispersion, on defining a zone averaged relaxation rate, $\tilde{\Gamma}$, an approximate non-Fermi-liquid form may be derived[7]:

$$\lim_{T \to 0} \frac{C}{T} = \tilde{\eta} \frac{2.25}{\tilde{\Gamma}_2 - \tilde{\Gamma}_1} \ln \left[\frac{\tilde{\Gamma}_2}{\tilde{\Gamma}_1} \right] \text{ J mol}^{-1} \text{ K}^{-2} \qquad (2.33)$$

where the coefficient $\tilde{\eta}$ expresses the effective fraction of modes per atom per polarization contributing to the integral, taking into account their distribution in reciprocal space. Assuming similar functional forms at finite temperature, the ratio C/T is dominated by the low-temperature behaviour of the relaxation rates. In the presence of dispersion, for distributions of the type shown in figure 2(c), the low-temperature behaviour of C/T is dictated by the approximately wavevector independent $\Gamma_1(T)$ and will be given by $\tilde{\Gamma}_1(T) \sim \Gamma_1(T)$ up to temperatures $k_B T \sim \Gamma_2(Q_0)$. In contrast, for a distribution of relaxation rates such as that in figure 2(b), the $\tilde{\Gamma}_1(T) \sim \Gamma_1(T)$ approximation will hold good only over a more restricted temperature zone. In general, the characteristic non-Fermi-liquid logarithmic divergence is recovered when $(\Gamma_2 - \Gamma_1) \sim$ constant, $\Gamma_2 \sim$ constant, and $\Gamma_1 \sim T$:

$$\frac{C}{T} = a - b \ln [T]. \qquad (2.34)$$

C/T saturates for conditions of composition, pressure, field, etc, where at sufficiently low temperature $\Gamma_1 \sim$ constant and $\Gamma_2 \sim$ constant, and in the case where $\Gamma_1 \approx \Gamma_2$ a return to Fermi-liquid behaviour occurs. Parenthetically, it is noted that, in the framework of a dynamical heterogeneity model where renormalization of the primary (magnetic) degrees of freedom occurs within fluctuations of a secondary field, C/T may have non-trivial corrections.

---

[7] The dependence on temperature of $\tilde{\Gamma}$ may not precisely follow that of Γ.

3. Illustration of the distributed-relaxation *ansatz* by example

The consequences of equation (1.1) are illustrated through analysis of inelastic neutron scattering and thermodynamic data. As a primary vehicle for this purpose we select the compound UCu_4Pd which, as will be seen, exhibits the simplest, local, type 2 response (figure 4(a)) and for which extensive inelastic neutron scattering and thermodynamic data sets are available [13, 31–35]. Comparisons are then drawn within the available literature for the non-Fermi-liquid compounds $CeCu_{5.9}Au_{0.1}$, representative of a mode-selected type 2 non-Fermi-liquid (figure 4(c)), and $La_{1.95}Ba_{0.05}CuO_4$, for which the available neutron data may be understood in terms of a wavevector averaged type 1 response (figure 3(c)). From these examples it will already be seen that, in contrast to the rather general forms in the thermal evolution of thermodynamic quantities, a *broad range* of qualitatively different spectral line shapes of the inelastic neutron scattering response have been reported as being characteristic of the non-Fermi-liquid phase.

Concerning the analysis of the neutron scattering spectra, we note the highly demanding nature of the experiments, either (a) because the temperature is low compared to the energy of excitation (Bose factor small for quantum fluctuations), (b) since the system is a long way from criticality (in composition, pressure, or wavevector) and the susceptibility is therefore small, or (c) because the frequency spectrum of the fluctuations demands high energy resolution which implies a reduced neutron flux. These factors have conspired in leading to the use of loose collimation and focusing optics to obtain a measurable signal; i.e. in the general use of poor q-resolution to maintain resolution in frequency (of interest in E/k_BT scaling). Thus in the analysis there are two issues. First an experimental question: that of the role of resolution and probe coherence in (q, ω) space. How much averaging has been carried out to obtain the spectrum and has it been adequately accounted for? The second is to model the distribution of relaxation times. Finally, having made the analysis, if the existence of an intrinsic distribution of relaxation rates is established, one may enquire as to its microscopic origin.

3.1. Analysis of UCu_4Pd

3.1.1. Inelastic neutron scattering spectra. In this intermetallic compound, based on the parent material, UCu_5, which is a Kondo-lattice antiferromagnet with a Néel transition at 16.5 K, substitution with palladium brings about a suppression of the antiferromagnetic state. The analysis of thermodynamic and transport properties has established non-Fermi-liquid behaviour and suggests the presence of a quantum critical state in the vicinity of $x = 1$ for $UCu_{5-x}Pd_x$ at low temperatures. The $x = 1$ composition has been selected on account of its stoichiometry; in addition, given the claim that even going to $x = 1.5$ does not qualitatively alter the form of the neutron spectra, the role of structural heterogeneity may not be decisive [13, 35]. The inelastic neutron data [13] have the following characteristics. First, beyond a gentle fall, which appears to be well accounted for by the uranium form factor, the spectra of $\chi''(q, \omega)$ are independent of q. Second, the low-energy position of the maximum in the line shape is incompatible, within the standard single-pole model of SED, equation (2.1), with the intensity distribution at higher energies. The frequency dependence is considered in [13, 31, 32] as having three qualitatively different regimes. The first distinction is for frequencies above or below $\omega^* = 25$ meV; then, depending upon the temperature, for $\omega < \omega^*$, one has frequencies much less than or far above k_BT. The focus of interest in the original work is given to truncated data sets satisfying $\omega < \omega^*$, i.e. ignoring the high frequencies, where the authors find an approximate scaling behaviour:

$$\chi''(\omega, T)T^{1/3} \approx (T/\omega)^{1/3}Z(\omega/T). \tag{3.1}$$
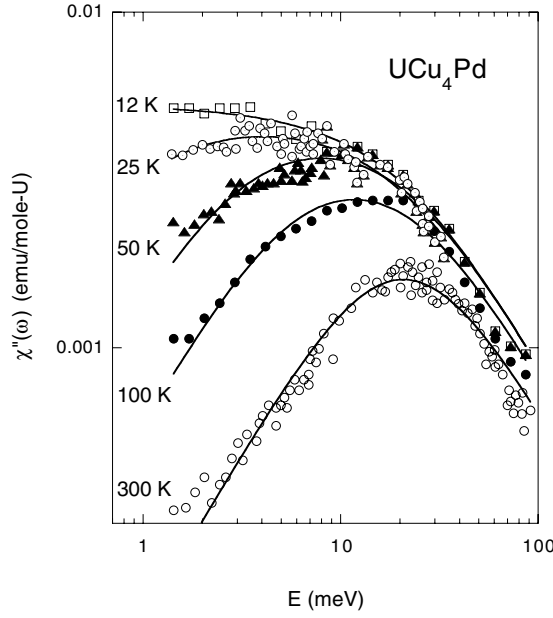
Figure 7. The dynamic susceptibility as measured in UCu$_4$Pd by means of inelastic neutron scattering [13] versus energy transfer for temperatures from 12 K to 300 K. The solid lines are fits to equation (2.4). In this figure the relative changes in *amplitude and form* over the full spectral range and for all given temperatures are represented by keeping Γ_2 constant and giving Γ_1 a linear temperature dependence, equation (3.2), as for the solid lines of figure 8.

Within the framework of the model susceptibility, equation (2.4), we find that *all* of the data given, i.e. over the full range of measured frequencies both above and below ω^* and at all temperatures, can be represented as shown by the solid lines in figure 7. The data have been analysed using equation (2.4) with u determined by the asymptotic slope at high frequencies (section A3.1 of appendix 3). Above 20 K one has the following simple parametrization of the fitted parameters[8] ($\pm 10\%$):

$$\Gamma_1 = 0.74 k_B (T - 1.2) \text{ meV}$$
$$\Gamma_2 = 18 \text{ meV} \tag{3.2}$$
$$A = 0.07/(\Gamma_2 - \Gamma_1) \text{ emu mol}^{-1}.$$

The simplicity of the parametrization of the response is remarkable. The scaling of A as the inverse of the difference of the relaxation rates reflects an approximate conservation of the area of the flat compact distribution over a significant temperature interval. This approximate conservation may be interpreted in an itinerant model, section 2.1, to reflect a local Fermi-liquid like (i.e. $T \ll T_{\text{Fermi}}$) response. The temperature dependence of Γ_1, Γ_2 is given in figure 8. As shown in the main figure, the estimated lower bound Γ_1 at 12 K becomes very small, which may indicate that, despite the suppression of the phase transition to $T = 0$ K, the dynamical response of the doped material 'remembers' the critical point of its host UCu$_5$ ($T_{\text{Néel}} \sim 16$ K). As increasing thermal energy overwhelms residual magnetic correlations, one anticipates a return to Korringa like behaviour as in figure 2(b$_1$). This is marked by the convergence of Γ_1

---

[8] This simplified parametrization for Γ_1 is not reliable much below 20 K since the value at 12 K is small and poorly defined (data do not extend low enough in energy; see figure A3, later). More details of the low-temperature values may be extracted from bulk measurements (section 3.1.3, section 3.1.4).
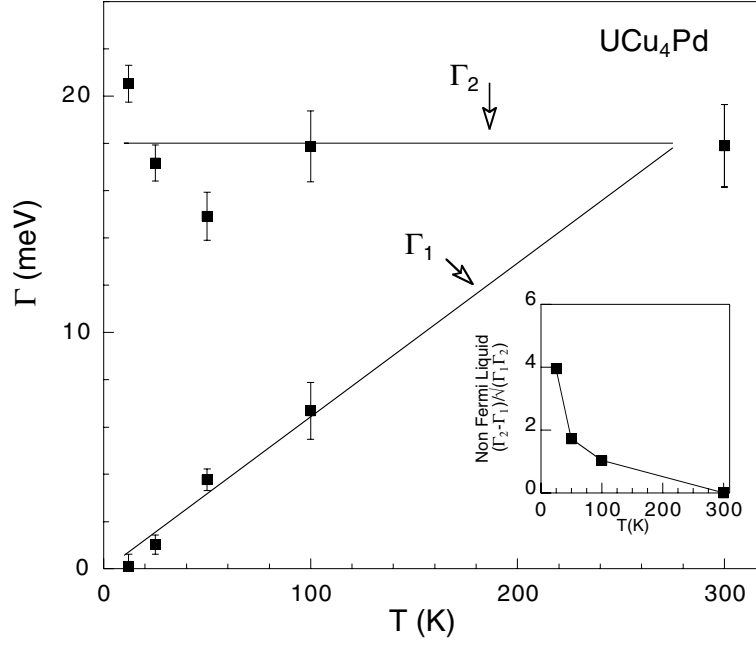
Figure 8. The dynamic susceptibility in UCu$_4$Pd has been fitted to equation (2.4) with u determined by the asymptotic slope at high frequencies, equation (A3.1), and may be represented as $u(T) = u(1 - (T/T_F)^2)$ with $u = 0.067 \pm 0.001$ meV emu (mol U)$^{-1}$ and $T_F = 700 \pm 20$ K. The inset gives the non-Fermi-liquid parameter deduced from inelastic neutron scattering data as a function of sample temperature for UCu$_4$Pd. The rise with falling temperature is indicative of a crossover from Fermi-liquid like behaviour at room temperature to non-Fermi-liquid tendencies.

and Γ_2 around 300 K; i.e. the bounds of $D(\Gamma)$ merge and the flat compact distribution reduces towards a Dirac function. The thermal evolution of the non-Fermi-liquid parameter is given in the inset to figure 8, where it shows a characteristic divergence towards low temperature.

Concerning the magnitudes of the bounding relaxation rates, we note that in the standard model of local SED where the q-dependence of χ may be ignored, the most probable[9] mode satisfies an equation of the form

$$\Gamma = u\mathcal{C}^{-1}k_B(T - T_1) \tag{3.3}$$

with a Curie constant

$$\mathcal{C} = \frac{Np^2\mu_B^2}{3V}$$

where u is a measure of the inverse transit time of the fermion quasiparticles taking part in the spin relaxation. This may be estimated as γQ where γ has the nature of a typical transport velocity and Q is a measure of the inverse relaxation distance. Assembling the constants one obtains

$$\Gamma = 5.6 \times 10^3 \frac{\gamma Q}{np^2}k_B(T - T_1) \tag{3.4}$$

[9] The most probable mode is not necessarily that observed; it depends upon the space-time scale of the experimental technique (e.g. x-ray, neutron, and thermodynamic probes may give very different results). However, in the regime of SED, i.e. away from critical or non-Fermi-liquid behaviour, the most probable is, in general, the most correlated mode of longest lifetime.

where γQ and $k_B T$ are in meV, n is the magnetic particle density in units of 10^{22} cm^{-3}, and p is the effective number of Bohr magnetons. Identifying the most probable mode with the mode of longest lifetime, in the presence of residual antiferromagnetic correlations, $Q \sim$ (U–U distance)$^{-1}$, $\gamma \sim (1\text{--}2) \times 10^{-3}$ meV Å (taken from previous analyses of paramagnetic materials [14, 15]), $n \sim 1\text{--}3$, and we find $p \sim 3.3\text{--}1.7$ in reasonable agreement with the measured moment. Some justification may come, as discussed in section A1.3 of appendix 1, from the perspective that the lowest relaxation rate may exhibit the strongest influence of residual antiferromagnetic correlations. Given the polycrystalline nature of the sample, one may question the role of an intrinsic anisotropy of $\chi(q, \omega)$ as the origin of the distribution of relaxation rates. Little can be said save that analysis of the bulk susceptibility in section 3.1.3, over a similar temperature interval, confirms the bounding temperature dependencies of the relaxation rates and the form of $D(\Gamma)$ as estimated from inelastic neutron scattering data. Since anisotropy is expected to become progressively more important with decreasing $|q|$, this makes it unlikely that it plays a major role.

3.1.2. Scaling of $\chi''(q, \omega)$ with $E/k_B T$. For UCu$_4$Pd, scaling of χ'' with $\omega/k_B T$ has been proposed with the scaling exponent $\alpha \sim 1/3$ for data sets with energy transfers below $\omega^* = 25$ meV [13]. Since the given analysis fits well to the whole data set at all measured energy transfers and all temperatures (figure 7), it is clear that within these bounds the analytical form, equation (2.4), will obey the chosen scaling relationship. Inspection of the fitted parameters, equation (3.2), indicates that the decision to treat $\omega < \omega^*$ in [13] neglects all data above Γ_2, i.e. ignores the $\alpha \to 1$ high-frequency asymptote anticipated from equation (2.4). In figure 9(a) a scaling plot of all the data for UCu$_4$Pd with $\alpha = 1$ is presented; the high-frequency data show good agreement with both the predicted scaling exponent and functional form, $g(\omega/k_B T) \to (\omega/k_B T)^{-1}$. The low-frequency condition of equation (2.4), $[k_B T]^{1+\alpha}/\Gamma_1\Gamma_2 = $ constant, may be approximately satisfied at any temperature when $\Gamma_1 \approx k_B T$ and $\Gamma_2 \approx$ constant for $\alpha = 0$, as shown in figure 9(b), or more generally solved graphically (in the vicinity of a given temperature) using the parametric values of $\Gamma_{1,2}$ to estimate the effective exponent as illustrated in figure 10. In figure 10 the scaling exponent taken over the range $0 < \alpha < 1$ (together with the value of the scaling constant c) required for approximate low-frequency scaling is given; optimum scaling occurs for low values of α. Since this semi-analytical method does not take into account the actual dynamic range of available data, the alternative empirical scaling criterion, equation (2.18), may in practice be more relevant. Application to data sets at the lowest and highest temperatures yields an effective exponent $\alpha \approx 0.7$ as illustrated in the figure 9(c). Finally, by way of example for three temperatures, 12 K, 100 K, and 300 K, in figure 9(d) the solid line illustrates the level of agreement attained on taking the functional scaling form previously proposed for CeCu$_{5.9}$Au$_{0.1}$ with the exponent $\alpha = 0.75$ [25].

3.1.3. $\chi(T)$ in UCu$_4$Pd. The measured bulk susceptibility in UCu$_4$Pd [33] is given in figure 11 as squares together with the response calculated with parameters from the neutron data analysis (dashed line) using equation (2.20):

$$\chi' = \frac{u/(k_B a)}{T_2 - T_1 - T} \ln\left[\frac{T_2}{T + T_1}\right]. \tag{3.5}$$

In the absence of a remarkable balancing of changes in spectral weight across the zone, the excellent agreement in the temperature dependence strongly supports the wavevector independent parametric form derived from the inelastic scattering. Extending the analysis to lower temperatures, the same functional form yields the solid line. Since no energies are
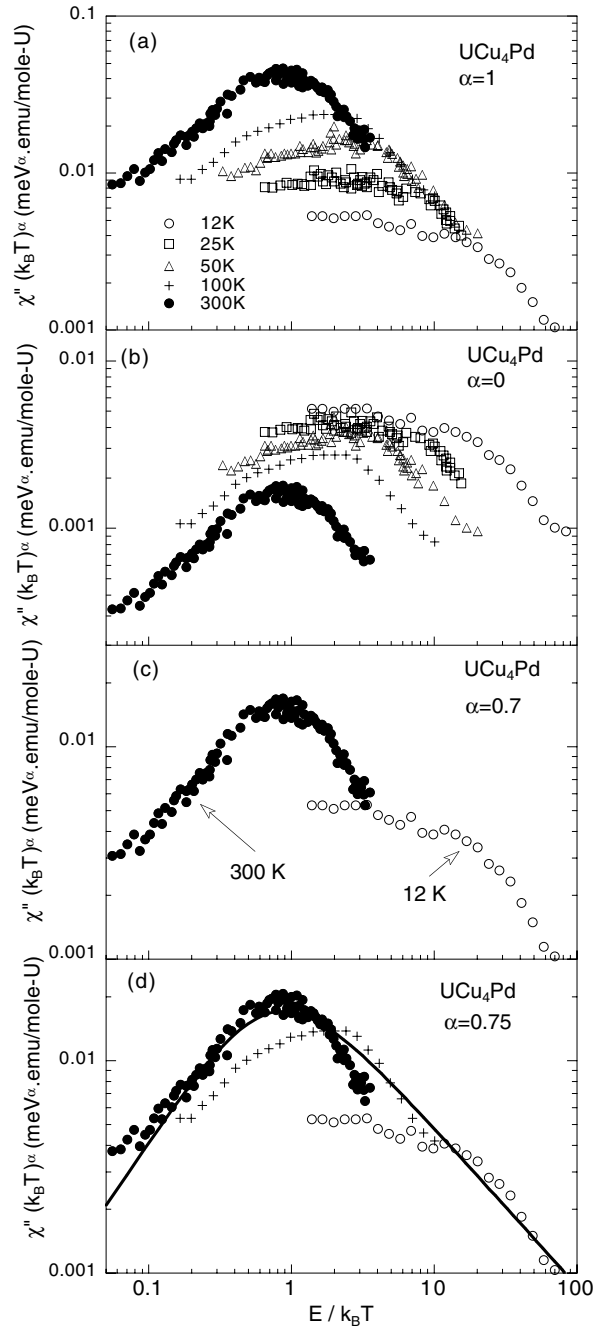
Figure 9. Going from double-logarithmic plots for UCu$_4$Pd, figure 7, to scaling plots. In frame (a) all data are replotted with E/k_BT as abscissa and $\chi''k_BT$ as ordinate. It is evident that no scaling like plot exists except for data taken in the high-frequency limit where the response is unrenormalized. In frame (b) an approximate scaling for data taken in the low-frequency limit is obtained for $\alpha = 0$ (see also figure 10). In frame (c), using the criterion given in equation (2.18), which yields $\alpha \sim 0.7$, an approximate scaling curve may be constructed. In frame (d), data at 12 K, 100 K, and 300 K for UCu$_4$Pd are plotted following the scaling relation suggested in [25]. The solid line follows equation (4) of [25]. In this form, a closer agreement with the data can be obtained since the abscissa scaling has been relaxed to $E/(ak_BT)$.
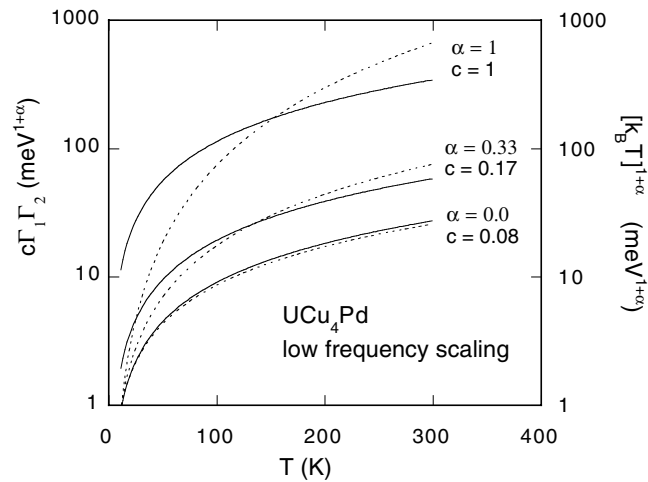
Figure 10. Plots used to estimate the scaling exponent for data obtained in the low-frequency limit of equation (2.4). The graphical solution to the equation $[k_B T]^{1+\alpha}/\Gamma_1\Gamma_2 = \text{constant}$ is given for $0 < \alpha < 1$. The solid and dotted lines represent $c\Gamma_1\Gamma_2$ and $[k_B T]^{1+\alpha}$ respectively; optimum scaling occurs over the temperature range of closest overlap.
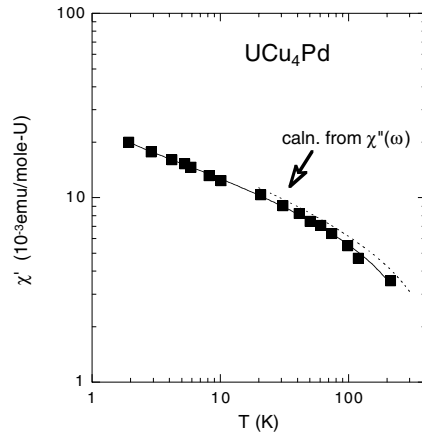

Figure 11. The measured bulk susceptibility in UCu$_4$Pd [33] (squares) and the response calculated from the neutron data (dashed line) using equation (3.5). The solid line is a fit to the same form. Since no energies are resolved in this technique, only the Curie ratio $u/(k_B a)$ may be determined. The parameter values, with the estimates from inelastic neutron scattering above 12 K given in square brackets, are: $u/(k_B a) = (840 \pm 70) \times 10^{-3}$ emu mol^{-1} [$(1040 \pm 100) \times 10^{-3}$ emu mol^{-1}]; $T_1 = -0.7 \pm 0.2$ K [1.2 ± 0.3 K]; $T_2 = 255 \pm 40$ K [280 ± 30 K]. On taking $a_1 = 0.74$ (neutron value, equation (3.2)), estimates for relaxation rates may be given as $\Gamma_1 = 0.74 k_B (T - 0.7 \pm 0.2$ K) meV and $\Gamma_2 = 16.3 \pm 2.5$ meV.

resolved in this technique, only the Curie ratio $u/(k_B a)$ may be determined; the parameter values are given in equation (3.6) with estimates from inelastic neutron scattering above 12 K given in square brackets:

$$u/(k_B a) = (840 \pm 70) \times 10^{-3} \text{ emu mol}^{-1} \qquad [(1040 \pm 100) \times 10^{-3} \text{ emu mol}^{-1}]$$
$$T_1 = -0.7 \pm 0.2 \text{ K} \qquad\qquad\qquad [1.2 \pm 0.3 \text{ K}] \qquad\qquad\qquad\qquad (3.6)$$
$$T_2 = 255 \pm 40 \text{ K} \qquad\qquad\qquad\quad [280 \pm 30 \text{ K}].$$

On taking $a_1 = 0.74$ (neutron value, equation (3.2)), estimates for relaxation rates may be given as $\Gamma_1 = 0.74k_B(T - 0.7 \pm 0.2 \text{ K})$ meV and $\Gamma_2 = 16.3 \pm 2.5$ meV. There are no significant discrepancies in the parameters, given that T_1 is determined to much lower temperatures in the bulk measurements and, as was pointed out, is in any case poorly defined in the neutron data.

3.1.4. C/T in UCu_4Pd and NMR in $UCu_{3.5}Pd_{1.5}$. In figure 12 we plot C/T for UCu$_4$Pd [34] both in zero external field and under 6 T, as circles and triangles respectively. In the absence of evidence for strong anisotropy or dispersion, equation (2.30) is employed with the same functional form for $D(\Gamma)$ and bounding relaxation rates as were used in the analysis of the neutron spectra and the bulk susceptibility. For $B = 0$ T and $0.15 < T < 3$ K the solid lines in figure 12 show the results of analysis with $\Gamma_1 = a_1k_B(T - 0.005 \pm 0.006 \text{ K})$ meV, $\Gamma_2 = 1.1 \pm 0.05$ meV, and $\eta = 0.060 \pm 0.003$ given $a_1 = 0.74$ (neutron scattering value). The small value of η reflects a quenching of magnetic relaxational degrees of freedom over the measured temperature interval. One possibility is to equate this with a reduced number of magnetic ions, i.e. roughly 6% of the uranium ions are excited in (magnetic) relaxational processes on the space-time scale of the experiment. The implied (dynamic) heterogeneity of relaxation sites might then be interpreted as arising from an incomplete (i.e. exhaustion of Kondo) screening [12, 13, 33]. On the other hand, the coincidence of the ~15-fold reduction in both the upper bound, Γ_2, and η strongly suggests that, at low temperature, the progressive renormalization of $D(\Gamma)$ seen below 300 K is compounded with a loss of spectral weight in relaxation modes of characteristic frequency above $\sim k_B T_{\text{Néel}}/\hbar$. Such modes, which see very weak renormalization, are neglected in the calculation of C/T. Further low-temperature quenching of modes is evidenced by the flattening of C/T below ~0.15 K.

Under an applied field of 6 T there is a marked reduction of the heat capacity below ~1.5 K. Since the field suppression of (antiferromagnetic) fluctuations is expected to be most marked for
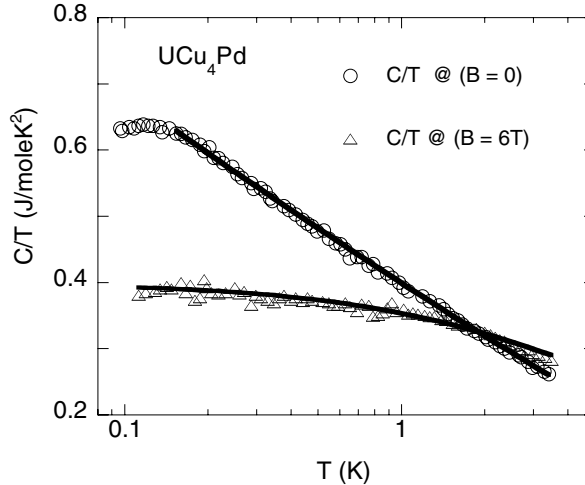

Figure 12. The linear coefficient of the heat capacity at low temperature in UCu$_4$Pd versus T; circles and triangles are for $B = 0$ and $B = 6$ T respectively [34]. The solid line is a fit to the functional form of equation (2.30) for $B = 0$ T and $0.15 < T < 3$ K with $\Gamma_1 = a_1k_B(T - 0.005 \pm 0.006 \text{ K})$ meV, $\Gamma_2 = 1.1 \pm 0.05$ meV, and $\eta = 0.060 \pm 0.003$ given $a_1 = 0.74$ (neutron scattering value). The small value of η reflects an effective quenching of magnetic relaxational degrees of freedom. For $B = 6$ T, Γ_2 is kept fixed, giving: $\Gamma_1 = a_1k_B(T + 2.8 \pm 0.1 \text{ K})$ meV and $\eta = 0.084 \pm 0.001$. See section 3.1.4 for a discussion.

the low-energy modes, Γ_2 is kept fixed in the analysis, giving: $\Gamma_1 = a_1 k_B (T+2.8\pm0.1 \text{ K})$ meV and $\eta = 0.084 \pm 0.001$. The key change lies in the reduced bandwidth of the relaxation rates, i.e. the return towards a Fermi-liquid like response, as reflected in the fall of the Curie–Weiss temperature from ~ 0 K to ~ -3 K. In this context we recall the nuclear spin-resonance results (under an applied field of 5 T) for $UCu_{3.5}Pd_{1.5}$ [35] which, together with the dynamical susceptibility ($B = 0$ T), fail to find an explanation within the Kondo-disorder distributed-temperature model [12–13, 31–35] and for which the main conclusions are: (i) that the NMR data under applied field may be most efficiently represented by a single effective relaxation time; and (ii) that there is an initial linear temperature dependence of $\theta_1^{-1}(T)$, figure 4 [35], for 0.1 K $< T < 3$ K. Both results may be understood in the light of the analysis of C/T data under a 6 T applied field from which the following can be inferred; (i) the collapse of the distribution $D(\Gamma)$; and (ii) a break point from linear to sublinear temperature dependence of $\theta_1^{-1}(T)$ at $T_1 = 2.8$ K for $\Gamma_2 \sim$ constant (equation (2.26)). The agreement between NMR and C/T analyses demonstrates an insensitivity of the global non-Fermi-liquid behaviour in $UCu_{5-x}Pd_x$ to exact composition and accompanying defect structure, suggesting an intrinsic mechanism in agreement with conclusions drawn from inelastic neutron scattering experiments on both UCu_4Pd and $UCu_{3.5}Pd_{1.5}$ [13, 31, 32].

3.1.5. Summary of results on UCu₄Pd. To conclude this section, we summarize our findings on UCu_4Pd where the unusual frequency dependence of the inelastic neutron scattering data appears to reflect type 2 behaviour. The thermal evolution of the parameters Γ_1 and Γ_2 implies, first, that above the characteristic temperature ~ 300 K, this system should behave as a simple paramagnetic relaxor, $\Gamma_1 \sim \Gamma_2 = \Gamma$. Exploiting the q-independence of the data, an estimate of Γ_1 can be made which appears to be in accord with the experimental value and suggests that, whilst long-range (phase) correlations have been lost, a residue of the antiferromagnetism remains in the local, low-frequency dynamics on approaching the quantum critical composition. Since UCu_4Pd has no transition at low temperatures, Γ_1 is assumed to retain a finite value. Whilst this is consistent with analysis of thermodynamic properties, unfortunate problems of experimental resolution hinder direct evaluation using the neutron scattering data (the limited low-energy data at 12 K give $\Gamma_1 \sim 0.03\pm0.1$ meV on direct application of equation (2.4); using the saturation value, equation (A3.7), and estimating the position of $\sqrt{(\Gamma_1 \Gamma_2)}$ graphically yields 0.1 ± 0.1 meV). The constancy of u: (i) strongly suggests that the distribution of relaxation rates is unlikely to involve a mixture of different physical processes; and (ii) implies self-consistent renormalization in both amplitude and relaxation rate of the dynamical susceptibility (within a given fluctuation).

In the light of the these results, it is interesting to note that inelastic neutron spectra for polycrystalline samples of UCu_5 ($T_{\text{Néel}} = 16$ K) have been interpreted with two characteristic energy scales [36]; the first is a narrow (Gaussian) feature which peaks in intensity in the paramagnetic phase around 20 K with a width ~ 0.5 meV and appears to account for an excess intensity at low energies in the range of $|Q|$ of the antiferromagnetic wavevector; and the second is a broad (Lorentzian) component of ~ 10 meV width unaffected by the transition at $T_{\text{Néel}}$. The rapid increase in scattering cross section of the low-energy Gaussian component on cooling for 20 K $< T < 40$ K may be indicative of a build-up of phase coherence between dynamic, antiferromagnetically correlated blocks which eventually gives way to magnetic order below 16 K [37]. In figure 13 the values for the bounding relaxation rates in UCu_4Pd estimated from the neutron scattering and thermodynamic techniques are given, as are the values of the Gaussian and Lorentzian features of the host compound UCu_5. The substantial agreement between the findings for these compounds suggests a continuity of physical properties. In particular, the transfer of spectral weight out of the

(q, ω) correlated Gaussian mode in the paramagnetic phase of UCu_5 into the wavevector independent distribution $D(\Gamma)$ of UCu_4Pd may be seen as a process of localization in space and time of the magnetic fluctuations on passing to the non-Fermi-liquid phase. This space-time fragmentation of antiferromagnetic fluctuations is consistent with the increasing role of phase-incoherent, dynamical heterogeneities, being determinant in the properties of the non-Fermi-liquid phase as reflected in the analyses by the loss of low-frequency correlations which become renormalized into modes of increased relaxation rate.
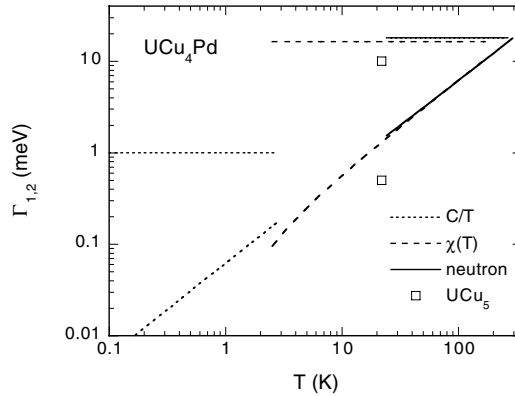

Figure 13. The values for the bounding relaxation rate in UCu_4Pd estimated from neutron scattering, $\chi(T)$, and C/T results given as the solid, dashed, and dotted lines respectively. The corresponding values estimated from the measured Gaussian (low-energy temperature-dependent) and Lorentzian (high-energy temperature-independent) components in UCu_5 [22] are given at 20 K as open squares.

Bringing together the results obtained from the analysis of neutron scattering data and the heat capacity, a change of regime appears around $T_{Néel}$ for the host. Above $\sim$20 K the characteristic speed-up and redistribution in momentum space of relaxation modes is in accord with the general suppression of susceptibility on passing from UCu_5 to the non-Fermi-liquid composition. The presence of an incipient phase transition in the non-Fermi-liquid phase below $\sim T_{Néel\,host}$ involves the loss of short-timescale (and short-spatial-scale) modes (as determined in the analysis of the heat capacity, figure 13) down to the frequency of $\sim k_B T_{Néel}/\hbar \sim 1$ meV. This supports the notion that a bulk (quantum) critical point, at which the timescale (and spatial scale) of persistent magnetic order diverges, may be identified as the point of formation of stationary mean-field phase coherent feedback [37]. The increased role of (antiferro-) magnetic correlations inferred at low temperature may be anticipated to be marked by a developing magnetic structure factor. Such a focusing of response in reciprocal space would also contribute to a reduction in the coefficient η as estimated by the C/T ratio. Application of a magnetic field acts in some sense in the opposite direction to lowering the temperature, as it selectively freezes the lowest-energy modes leading to a Fermi-liquid like response associated with a relatively high characteristic relaxation rate and hence low C/T. Further understanding may come on extending neutron scattering data to lower temperatures and frequencies under variable magnetic field.

3.2. Analysis of $CeCu_{5.9}Au_{0.1}$

3.2.1. Analysis and scaling of inelastic neutron scattering spectra. $CeCu_{5.9}Au_{0.1}$, based on the host compound $CeCu_6$, has been established as one of the archetypal non-Fermi-liquid

compounds in view of its thermodynamic and transport properties. Interesting questions have been posed as to its situation in the vicinity of an antiferromagnetic QCP with the host material considered as exhibiting a nearly ideal Fermi-liquid state [38]. The inelastic spectra [25, 39, 40] are presented at very low energy transfer at low temperature. The position of the maximum in the energy response at fixed wavevector transfer appears incompatible, within a single-pole model, with the intensity distribution at higher energies. That is, it appears not to be possible to fit simultaneously the sharp rising edge at the lowest frequencies with the slow falling tail to the standard paramagnetic form. One *ansatz*, as adopted in [25], is, in the vicinity of the critical wavevector, to soften the frequency exponent in the standard model from 1 to an experimentally determined value $\alpha < 1$:

$$\chi(\omega; T) = \left[\frac{\Gamma \chi(T)}{\Gamma - i\omega} \right]^{-\alpha}. \tag{3.7}$$

In general, the smaller the coefficient α, the slower the high-frequency fall off of the dynamical susceptibility, thus giving rise to the desired line shape. Despite the strong dependence of the magnetic response on wavevector (see figures 1 and 2 of [25]), resolution corrections are asserted to play a negligible role [25, 40].

The measured inelastic response in $CeCu_{5.9}Au_{0.1}$ may be readily interpreted in terms of equation (2.4), as given by the solid lines in figure 14. From the good fits obtained, it is evident that the analytical results will conform to the scaling law proposed in [25] with $0.75 < \alpha < 0.8$; indeed the distributed-relaxation rate model is able to account for the systematic divergences present in the data from the generalized scaling law. Analysis of the data presented, taken in the vicinity of the magnetically soft point in the Brillouin zone, indicates an approximately linear temperature dependence of Γ_1 with saturation of Γ_2 to the lowest temperature measured which suggest that the sublinear value of the scaling exponent may be rationalized as in section 2.4. In a similar light, the use of ω/aT as the scaling variable in [25] with $a = 0.82 k_B$ may be seen (equation (2.11)) as a step towards scaling in ω/Γ_1 (see also section 3.3.1). Parametric values for $\Gamma_{1,2}$ are displayed in the inset to figure 14 (left-hand ordinate) and given in the caption; the value $T_1 \sim 0$ drives a diverging non-Fermi-liquid parameter (inset to figure 14, right-hand ordinate). Nevertheless, given the tendency towards low-temperature saturation of $\Gamma_2 \sim 2$ K and recalling that both the Kondo temperature of $CeCu_6$, ~ 2 K, and $T_{Néel} \sim 2.2$ K for the antiferromagnetic compositions with $x > 0.1$ are already low, it appears that experiments may have to be carried out to still lower temperature (mK) to establish the presence of a possible QCP.

3.2.2. Thermodynamic properties of $CeCu_{5.9}Au_{0.1}$.   The experimental low-temperature ratio C/T is given in figure 15(a) by the open circles [41]. On account of the strongly dispersive response, we have made a fit using equation (2.33), as indicated by the solid line. The bounding relaxation rates given by the analysis of neutron scattering data, i.e. the dashed lines in the inset to figure 14, yield the (temperature-independent) coefficient $\tilde{\eta} = 0.137 \pm 0.001$. Since the $\Gamma_{1,2}$ distributions determined by means of neutron scattering and analysis of C/T agree, and the dominant fluctuations are concentrated in a small volume of (quasi-$2d$) momentum space around the antiferromagnetic wavevector, the overall distribution of relaxational modes is anticipated to be similar to that of figure 2(c).

To gain information on the renormalization of long-wavelength relaxation rates away from the antiferromagnetic zone centre, which dominates both the neutron scattering response and low-temperature heat capacity, the thermal evolution of the bulk susceptibility has been examined. Within the context of equation (2.20) a good description of the available data is possible, as demonstrated by the solid line in figure 15(b) where the open squares represent
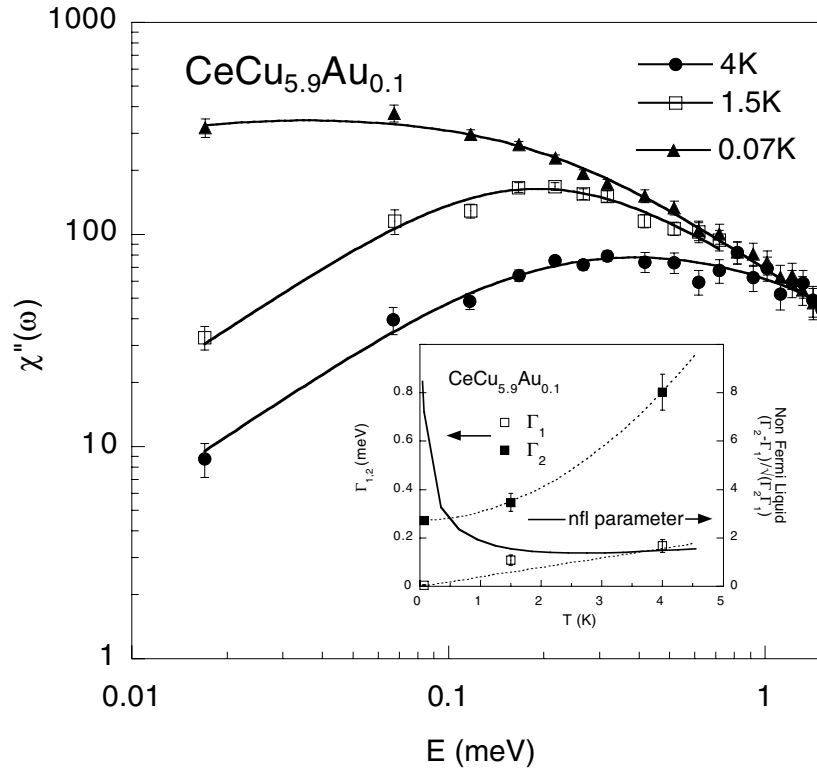
Figure 14. The dynamic susceptibility measured in $CeCu_{5.9}Au_{0.1}$ by means of inelastic neutron scattering [25] plotted on double-logarithmic axes. The solid lines are fits to equation (2.4) discussed in section 3.2.1. The inset gives the parameters for $CeCu_{5.9}Au_{0.1}$ derived from fits to equation (2.4) (left-hand ordinate). The dashed lines show the parametric values of $\Gamma_{1,2}$ used in the analysis of C/T: $\Gamma_1 = 0.456k_B(T - 0.026)$ meV; $\Gamma_2 = 0.271 + 0.001\,67\,T + 0.0328\,T^2$ meV. The non-Fermi-liquid parameter, equation (2.9) (right-hand ordinate), is represented as a solid line based on the parametric values (dashed lines) for lower and upper limits, Γ_1, Γ_2, of the distribution $D(\Gamma)$. Interestingly, the non-Fermi-liquid parameter varies over similar ranges in this material and UCu_4Pd (figure 8), despite the different temperature scales and relaxation processes, which are strongly dispersive in the former and localized in the latter.

the measurements performed at 0.1 T [41]. The solid line is calculated in the units of [41] with the following parametric values: $u/k_Ba = 1.51 \pm 0.02$; $\Gamma_1 \propto (T + 0.82 \pm 0.02$ K); $\Gamma_2 \propto (T + 23.6 \pm 0.5$ K).

3.2.3. Summary of results on $CeCu_{5.9}Au_{0.1}$. In figure 16 we summarize our findings for the bounding relaxation rates $\Gamma_{1,2}$. The magnitudes of the points represented by open circles and squares, for Γ_1 and Γ_2 respectively, have been determined directly by analysis of neutron scattering data. The solid lines indicate the values of $\Gamma_{1,2}$ used to analyse the low-temperature heat capacity with one temperature-independent amplitude, i.e. the effective mode density, as a parameter. The good agreement over the measured temperature interval in figure 15 supports the validity of this parametrization. Finally, since the thermodynamic susceptibility involves the integral over all $q = 0$ excitations, i.e. the experimental technique has no intrinsic energy resolution, the measured temperature dependencies of $\chi_{1,2}$, as determined in figure 15(b), have tentatively been converted to $q = 0$ relaxation rates using the measured neutron prefactor,
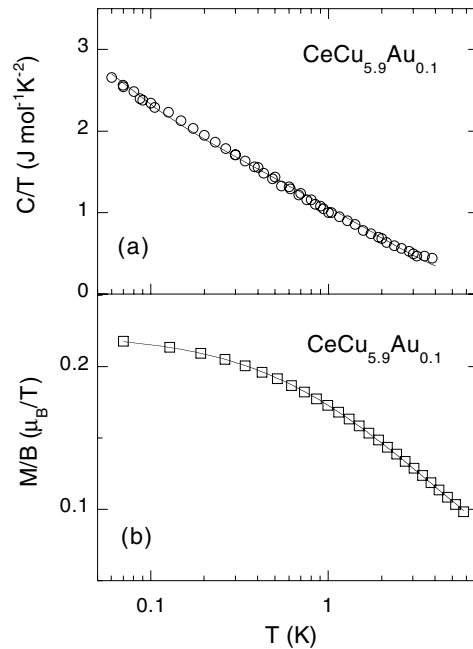
Figure 15. (a) Experimental values for C/T in CeCu$_{5.9}$Au$_{0.1}$ versus T [41]. The solid line is calculated from equation (2.33) with the following amplitude coefficient and bounding relaxation rates: $\tilde{\eta} = 0.137 \pm 0.001$; $\Gamma_1 = 0.456 k_B (T - T_1)$ meV, with the value derived from C/T of $T_1 = 0.026 \pm 0.002$ K (a neutron scattering fit to three available data points gives $T_1 = -0.5 \pm 0.2$ K); $\Gamma_2 = 0.271 + 0.001\,67\,T + 0.0328\,T^2$ meV (from both neutron scattering and C/T). The inset to figure 14 gives the values of Γ_1, Γ_2 used in this analysis, as dashed lines. (b) Experimental values for $\chi(T)$ given as open squares [41]. The solid line is calculated after equation (2.20) with the following parametric values: $u/k_B a = 1.51 \pm 0.02$; $\Gamma_1 \propto (T + 0.82 \pm 0.02$ K); $\Gamma_2 \propto (T + 23.6 \pm 0.5$ K).
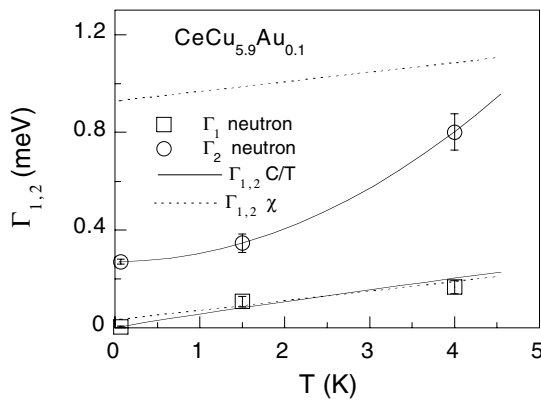
Figure 16. Summary of the bounding relaxation rates for $D(\Gamma)$ in CeCu$_{5.9}$Au$_{0.1}$. The points are determined by analysis of inelastic neutron scattering data, the solid lines from C/T, and the dashed lines estimated from the bulk susceptibility using the measured neutron prefactor, $a_1 = 0.456$.

$a_1 = 0.456$, and are given as dashed lines in figure 16. The implied suppression on cooling of the upper relaxation rate around the antiferromagnetic wavevector (i.e. the difference between upper dashed and solid lines) suggests that, whilst above $\sim$4 K the magnetic response may approach (quasi-) local, q-independent behaviour for the full spectrum of relaxation modes, at low temperature an overall softening of the high-frequency spectrum occurs in the vicinity

of Q_{afm}. A similar situation to that in UCu_4Pd may then pertain, where, for $T > T_{\mathrm{N\acute{e}el\,host}}$, the response is dominated by an approximately local distribution $D(\Gamma)$ which may condense around the residual antiferromagnetic correlations in the low-temperature limit.

In this context it is illuminating to recall that the quasielastic response of the non-magnetic host, $CeCu_6$, has been interpreted with a linewidth that is approximately constant at low temperature ($\Gamma \sim 0.5$ meV) and rises as $\sqrt{T}$ above 3 K to reach ~ 1 meV at 10 K [22] (i.e. of the form anticipated in figure 2(b)). The magnitude and thermal evolution of the linewidth in the *non-magnetic* host are thus very close to those estimated around $q = 0$ in $CeCu_{5.9}Au_{0.1}$ in the SED approximation, $\Gamma_{\mathrm{para}} = \sqrt{(\Gamma_1\Gamma_2)}$, using the bulk susceptibility values of $\Gamma_{1,2}$. This too is consistent with modest renormalization of relaxation rates at long wavelengths on passing to the $CeCu_{5.9}Au_{0.1}$ composition. These observations suggest that the passage from paramagnetic $CeCu_6$, via the critical composition, to the magnetic state for Au concentrations >0.1 is signalled by an overall softening of the lowest relaxation rate at the critical composition and accompanied by the selective quenching of high-frequency modes around the incipient antiferromagnetic wavevector (as in figure 4(c)). We now turn to the heat capacity; equation (2.27) reproduces successfully the low temperature value of C/T in $CeCu_6$ on inserting the $q = 0$ values of $\Gamma_{1,2}$ estimated for $CeCu_{5.9}Au_{0.1}$ from the bulk susceptibility, supporting a global similarity in dynamics consistent with the interpretation of the temperature dependent relaxation rate. Furthermore, the low temperature amplification of C/T in $CeCu_{5.9}Au_{0.1}$ over $CeCu_6$, together with the small coefficient $\tilde{\eta}$ estimated in equation (2.33), implies a focusing of the non-Fermi-liquid fluctuations around the antiferromagnetic wavevector. These observations bolster the notion that on doping with Au, the major renormalization in the magnetic response is restricted to the vicinity of the soft wavevector, Q_{afm}, and stimulate further, direct, neutron scattering measurements of the mode structure in both critical and weakly antiferromagnetic compositions over a wide range of wavevectors and temperatures.

3.3. Doped rare-earth cuprates

3.3.1. Analysis of $La_{1.95}Ba_{0.05}CuO_4$. As the compound is a member of the family of high-T_c cuprates, its anomalous normal and superconducting properties have made it the focus of intensive investigation. This particular composition, lying between the antiferromagnetic and superconducting phases, exhibits an anomalous $\rho(T)$ with a rapid fall from low temperature to 50 K above which it increases in an approximately linear, non-Fermi-liquid like manner. This behaviour prompted the question as to whether, on doping, the material passes close to a QCP *en route* from an antiferromagnetic insulator through a spin-disorder phase to a superconductor [9]. The absorptive part of χ derived from the neutron data has an energy profile which exhibits a sharp rising edge at low temperature and then is almost energy independent up to 100 meV (figure 3 of [9]). The data follow a qualitatively different scaling function from the *ansatz* of Schröder *et al* [25] for which the high-frequency tail would require $\alpha \to 0$, which is incompatible with the sharp initial rise. Within our model form, the high-frequency tail suggests an effective roll-off frequency, Γ_2, above 100 meV whilst the change of slope with temperature of the onset of $\chi''(\omega)$, figure 17, suggests a small value for Γ_1 which increases with temperature. We find for the following temperature dependence for the model parameters:

$$\Gamma_1 = 0.51k_{\mathrm{B}}(T - 5) \text{ meV}$$
$$\Gamma_2 \sim 150 \text{ meV} \tag{3.8}$$
$$A \propto 1/(\Gamma_2 - \Gamma_1).$$

The data given (open circles) are well reproduced (solid lines) in the plots of figure 17. The characteristic temperature $T_1 \sim 5$ K, at which point in this simple model $\Gamma_1 = 0$, is a measure of the spin-disorder freezing temperature previously estimated as 8 K [9]. The extrapolated temperature for SED would be $\sim$2000–3000 K. Below this temperature, but sufficiently above 5 K, we can approximate the response as

$$\chi'' = A\left[\arctan\left(\frac{\omega}{0.51 k_B T} \right) \right] \tag{3.9}$$

giving a generalized $\omega/k_B T$ scaling behaviour. This preliminary analysis, which indicates that the spectral distribution of the data falls within the scope of our model function, has however ignored the important role of q-averaging in this experiment. The values of $\chi''(\omega)$ have been extracted as the result of a $2d$ integration in the a–b plane; we proceed to examine how such averaging may yield the generic functional form of equation (2.4).

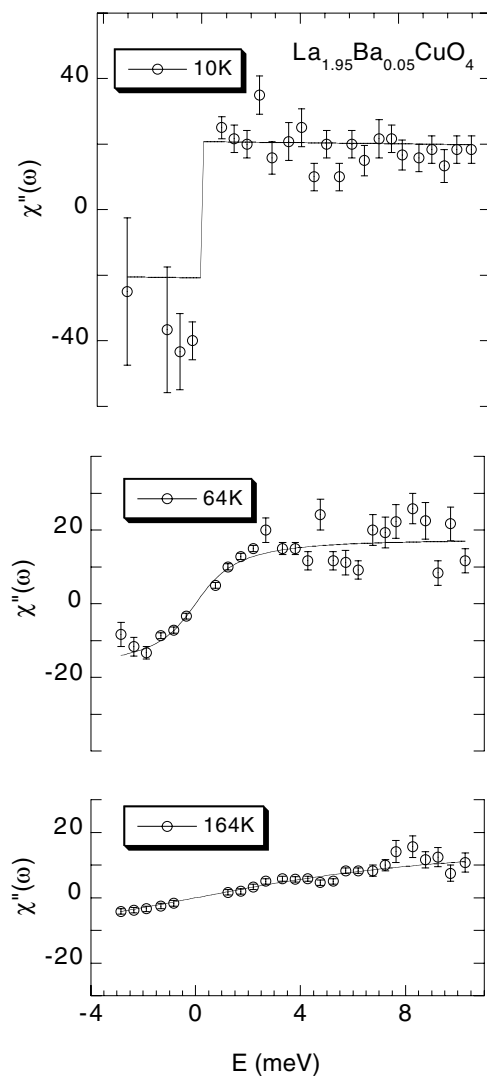**Figure 17.** The dynamic susceptibility estimated in $La_{1.95}Ba_{0.05}CuO_4$ by means of inelastic neutron scattering versus energy transfer at three temperatures [9]. The solid lines are fits to equation (2.4) discussed in section 3.3.1. The parametric values are $\Gamma_1 = 0.51 k_B (T - 5)$ meV and $\Gamma_2 \sim 150$ meV.

3.3.2. 2d q-space averaging in the analysis of $La_{1.95}Ba_{0.05}CuO_4$. We start by assuming SED

$$\chi'' = \frac{\omega \Gamma \chi}{\omega^2 + \Gamma^2} \tag{3.10}$$

that is type 1 behaviour with no intrinsic distribution of relaxation rates invoked, as in figure 3(c). What is measured (given the assumption of good energy resolution and loose q-resolution) is

$$\int \chi''(q, \omega) \, \mathrm{d}^d q = \int \frac{\omega \Gamma \chi}{\omega^2 + \Gamma^2} \, \mathrm{d}^d q \tag{3.11}$$

where d is the dimension of q-space integration performed in the experimental realization of $\chi''(\omega)$. The details of the calculation are given in appendix 2. In the case of a $2d$ integral about a critical wavevector (figure 2 of [9]), when $\chi(q)$ may be expressed in standard form, we obtain

$$\langle \chi'' \rangle_{2D} = \frac{\pi}{c} \left[\arctan\left(\frac{\omega}{\Gamma_1}\right) - \arctan\left(\frac{\omega}{\Gamma_1(1 + \lambda^2 Q^2)}\right) \right] \tag{3.12}$$

where $\chi(q)^{-1} = \chi^{-1} + cq^2$ and the correlation length λ has been introduced as $\lambda^2 = c\chi$. Since $\Gamma_1 = u\chi^{-1}(T)$, the form of Γ_1 (equation (3.8)) appears naturally if $\chi^{-1}(T)$ is of Curie–Weiss form with a critical temperature $T_1 \sim 5$ K, and the observation that Γ_2 is independent of temperature is recovered in the limit where $\lambda Q \gg 1$ (i.e. $Q \gg$ inverse correlation length), which yields $\Gamma_2 = ucQ_2^2$. For $u \sim \gamma Q$ (as in equation (3.4)) we obtain $\Gamma \sim 100$ meV using parameters not far from the canonical transition metal values, namely, $\gamma \sim 10^{-3}$ meV Å, $c \sim 10^5$ Å^2, and $Q \sim 1$ Å^{-1}. The evidence of dispersion (figure 2 of [9]) and the reasonable parameter values for the relaxation rate suggest that the $2d$ q-space integration may be critical in understanding the spectral form. This implies that, despite the anomalous spectral response and temperature dependence of $\rho(T)$, the underlying dynamics may be characterized by the canonical antiferromagnetic paramagnon form as found for example in $Cr_{1-x}V_x$ [16] and V_2O_3 [19].

In this context the NMR relaxation rates as a function of doping level and temperature in the related compound $La_{1-x}Sr_xCuO_4$ reveal an interesting behaviour. Analysis of the local response probed at NMR frequencies reveals the inferred width of the $D(\Gamma)$ distribution to be narrowest in the neighbourhood of the spin-disorder $x = 0.04$ composition. We consider this response in the following section.

3.3.3. NMR in $La_{2-x}Sr_xCuO_4$. Following equation (2.23), comparison with the data for $La_{2-x}Sr_xCuO_4$ given in figure 18 shows general agreement with the experimental situation [27, 42]. In detail, the fitted lines in figure 18 are based on equation (2.23) with Γ_1, Γ_2 of the form used in equation (2.21) assuming $a_1 = a_2$; the parametric values of T_1, T_2 are given in the figure caption. The inset of figure 18 gives the values of the deduced non-Fermi-liquid parameter as a function of temperature for each composition. The near-zero value for the Brillouin zone averaged NFL parameter of the $x = 0.04$ composition indicates the effective, local $D(\Gamma)$ to take on its narrowest distribution (i.e. approach simple paramagnon behaviour), as found in $La_{1.96}Ba_{0.04}CuO_4$, whilst at the doping level most favourable to superconductivity, $x = 0.15$, it manifests the broadest spectral distribution $D(\Gamma)$ with the strongest signature of the non-Fermi-liquid state.

4. Conclusions

The interface between experimental data and microscopic theory on low-energy phenomena may conveniently be made through the dynamical susceptibility. As outlined for a series of
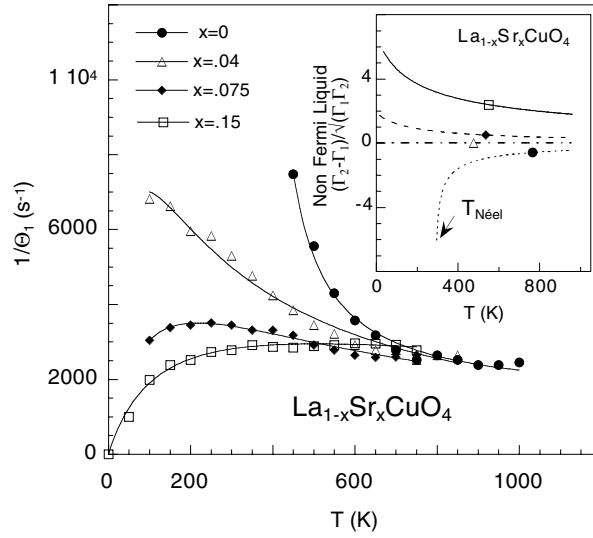
Figure 18. The inverse relaxation time in $La_{1-x}Sr_xCuO_4$ as a function of temperature for various compositions [27, 42]. The solid lines are fits to the equations discussed in section 3.3.3 with $a_1 = a_2$, $T_1 = -90$ K, and T_2 taking the values 286 ± 16 K, -90 ± 8 K, -500 ± 30 K, -4300 ± 1200 K for $x = 0.0, 0.04, 0.075, 0.15$ respectively. The inset gives the non-Fermi-liquid parameter for $La_{1-x}Sr_xCuO_4$ as a function of temperature for various compositions. The values for the antiferromagnetic ordering compound are characteristically negative and, at the spin-disorder composition, $x = 0.04$, the local response is indicative of a narrow effective distribution $D(\Gamma)$. On doping into the superconducting phase, the non-Fermi-liquid parameter increases to reach a maximum at optimum doping level and low temperatures.

exemplary materials in section 3, this enables a unified treatment of kinetic and thermodynamic properties in the non-Fermi-liquid state extending from the microscopic space-time scales probed by inelastic neutron scattering to the thermodynamic regime. The non-Fermi-liquid signatures are reproduced by generalizing the SED (Fermi-liquid) response to an incoherent sum of susceptibilities over a flat compact distribution, $D(\Gamma)$.

The approach may be seen as an extension of mean-field theory for the response function. From the refinement of the Curie–Weiss approach, to account for the presence of fluctuations on the average, homogeneous susceptibility in self-consistent approximations based on the scheme of Murata and Doniach [43], the renormalization is extended here to the local response function. Appropriate microscopic models for an interpretation of $D(\Gamma)$ revolve around the space-time filtering of the underlying fermion field with respect to the coherence volumes of both its elementary excitations and those of the experimental probe. In our treatment, the fermion field is eliminated in favour of a set of dissipative magnetization-density modes which provide the backcloth to models discussed in the text and appendix 1. The analyses given suggest an exquisite sensitivity of the response function to the local (magnetic) environment. The weak temperature dependence of Γ_2 indicates that the response on short timescales is not modified; thus the corrective terms, at least for materials not too far from a Fermi-liquid like regime, are essentially a low-frequency phenomenon and may therefore be mimicked within a renormalization scheme[10]. The concept of corrective terms local in space and

---

[10] With the caveat that application of renormalization in the vicinity of a QCP as $T \to 0$ assumes homogeneity of response to arbitrarily large space-time scales where a maximum sensitivity to the combined effects of heterogeneity and the intrinsic coherence volumes of the quantum field arises.

time, as an essential modification of the response up to mesoscopic length scales, gives interesting perspectives on a variety of phenomena; examples include structural and electronic supercooled liquid- and glass like phases, $(1/f)$ noise, the approach to the critical point, and the antiferromagnetic state [3–7, 37].

In conclusion, whilst the analysis of NER and the associated non-Fermi-liquid state relies only on development of equation (1.1), a semi-microscopic interpretation may be given in terms of spontaneous dynamical heterogeneities. The dual aspects of essential incoherence and local susceptibility renormalization within fluctuating space-time volumes are inferred from the simultaneous analysis of kinetic and thermodynamic data. It remains a challenge to extend thermodynamic and transport response theory to include the effects of both spontaneous dynamical heterogeneity and the space-time coherence properties of the elementary excitations and the probe; from the analogy with diffraction phenomena, one may anticipate a rich phenomenology based on the interplay of time and length scales [44].

It is hoped that the ideas and analyses developed may stimulate further experiments on these and related materials[11], thoughts on the possible role of spontaneous heterogeneity, and investigations of other, complementary scenarios for microscopic theories of the dynamical magnetic susceptibility in the non-Fermi-liquid state.

Acknowledgments

Appendix 1. Models for $D(\Gamma)$ in non-Fermi-liquids

A1.1. Introduction

Empirical evidence, based on the analysis of neutron scattering and thermodynamic measurements, suggests a generic NER (non-Fermi-liquid) susceptibility of the model form

$$\chi(\omega) = \frac{u}{\Gamma_2 - \Gamma_1} \ln\left[\frac{\Gamma_2 - i\omega}{\Gamma_1 - i\omega}\right] \tag{A1.1}$$

where Γ_1, Γ_2 are lower and upper bounds on the relaxation-rate distribution. Considerable experimental evidence also exists for a continuous transition between the non-Fermi-liquid and Fermi-liquid states, for example with varying temperature, through doping, under applied hydrostatic pressure, or under the application of a field. The smooth transition between equation (A1.1) and the susceptibility of SED:

$$\chi(\omega) = \frac{u}{\Gamma(q) - i\omega} \tag{A1.2}$$

may be effected through the following integral representation of χ:

$$\chi(\omega) = \int d\Gamma \, D(\Gamma)\chi(\Gamma; \omega) \tag{A1.3}$$

where the *distribution* $D(\Gamma)$ has the flat compact/Dirac form in the non-Fermi/Fermi-liquid case respectively. Thus, in the non-Fermi liquid at each wavevector, there is not just one

---

[11] The distribution $D(\Gamma)$ is not restricted to magnetic relaxation mechanisms; examples include electric field gradient relaxation as detected by means of NQR, quadrupole or orbital relaxation, or (anti-) ferroelectric relaxation, etc.

relaxation rate, but rather a distribution, $D[\Gamma(q)]$. At a formal level, the requirement of equation (1.1) to yield $\chi''(\omega)$ as in equation (2.4) (as is empirically verified by neutron scattering) is only that $D(\Gamma)\Gamma\chi_\Gamma = $ constant. In addition to arguments of self-consistency, i.e. the relaxation rate determines and is determined by the local susceptibility, and continuity to the Fermi-liquid phase, the choices $\Gamma\chi_\Gamma = u$ and $D(\Gamma) = 1/(\Gamma_2 - \Gamma_1)$ appear unique in being able to give, at the same time, an explanation of both the inelastic neutron scattering data and the thermodynamic properties. For example, at a given temperature, setting $\chi_\Gamma = $ constant, independent of Γ, could give an empirically correct form of $\chi''(\omega)$ for the interpretation of inelastic neutron scattering data on taking $D(\Gamma) \propto 1/\Gamma$ but at the expense of the self-consistent renormalization of the local amplitude and relaxation rate, and a low-temperature limit to C/T given by

$$\frac{C}{T} \approx \frac{1}{(\Gamma_2 - \Gamma_1)} \frac{1}{\ln(\Gamma_2/\Gamma_1)} \tag{A1.4}$$

which would be incompatible with the observed divergences.

To further the analysis of data, it is useful to distinguish the following scales of space and time in an experiment:

(a) sample:

- $V_{\text{sample}}, T_{\text{sample}}$: volume and lifetime of sample (metastable electronic or structural states);
- v_i, τ_i: volume and timescale of (dynamic) heterogeneity (of ith microregion);
- $\zeta, \Gamma^{-1}(q)$: space-time correlation scales of fluctuations;

(b) probe:

- $V_{\text{expt}}, T_{\text{expt}}$: experimental (probe) volume and timescale;
- $v_{\text{probe}}, t_{\text{probe}}$: effective neutron/photon/quasiparticle coherence volume and time.

When not dealing with kinetic effects or metastable glass like states the sample variables, V_{sample} and T_{sample}, may be eliminated in favour of V_{expt} and T_{expt}. The effective probe coherence takes into account the overlap of incident and scattered probe coherence volumes and is designated v_{probe} and t_{probe}. It gives the maximum characteristic scales of space and time that can be resolved, i.e. $\zeta v_{\text{probe}}^{-1/3} < 1$ gives the maximum correlation length and $\Gamma_{\text{min}}t_{\text{probe}} > 1$ gives the minimum Γ in $D(\Gamma)$ that can be resolved. The interplay of sample and probe space-time scales defines nine experimental regimes, given in table A1, whose leading elements are illustrated in figure A1, upper frame (space) and lower frame (time). Within each category, due attention must be paid that the relaxation rate and correlation length lie within the experimental resolution. In the case where the relaxation rates are dispersive, a type 1 distribution may be generated by augmenting the angular wavevector averaging which takes place over the experimental volume with explicit summations of recorded spectra.

A1.2. Type 1 distributions

Categories (3), (6), (9): in the category (9) phase with a dispersive (anisotropic) response, $\Gamma(q)$ is invariant over V_{expt} and T_{expt}. Averaging over V_{expt} (q-averaging) gives rise to $D(\Gamma)$ under the implicit assumption that v_{probe} and t_{probe} are large enough to resolve ζ and $\Gamma(q)$ respectively. Under categories (3), (6), gradients in temperature, pressure, doping, or intrinsic entropy-driven microscopic twinning, vacancy and defect-density variations (which may develop a quasiperiodic nature as in spinodal decompositions) give rise to a distribution of relaxation rates which are averaged over by V_{expt} with the implicit assumption that v_{probe} and t_{probe} are large enough to make the measurement.

Table A1.

	$\tau_i < t_{\mathrm{probe}} < T_{\mathrm{expt}}$	$t_{\mathrm{probe}} < \tau_i < T_{\mathrm{expt}}$	$t_{\mathrm{probe}} < T_{\mathrm{expt}} < \tau_i$
$v_i < v_{\mathrm{probe}} < V_{\mathrm{expt}}$	(1) Coherent spatial sum, averaged over V_{expt}; coherent temporal sum, averaged over T_{expt}	(2) Coherent spatial sum, averaged over V_{expt}; incoherent temporal sum over T_{expt}	(3) Coherent spatial sum, averaged over V_{expt}; static
$v_{\mathrm{probe}} < v_i < V_{\mathrm{expt}}$	(4) Incoherent spatial sum over V_{expt}; coherent temporal sum, averaged over T_{expt}	(5) Incoherent spatial sum over V_{expt}; incoherent temporal sum over T_{expt}	(6) Incoherent spatial sum over V_{expt}; static
$v_{\mathrm{probe}} < V_{\mathrm{expt}} < v_i$	(7) Homogeneous; coherent temporal sum, averaged over T_{expt}	(8) Homogeneous; incoherent temporal sum over T_{expt}	(9) Homogeneous; static

A1.3. Type 2 distributions

Categories (1), (2), (4), (5), (7), (9): for simplicity, the homogeneous slow mode, category (7), is detailed—that is, the relaxation rate is taken to be invariant over V_{expt} and $\tau_i < t_{\mathrm{probe}}$. This artificial restriction, like that of the frozen dynamical heterogeneity model considered in section 2.2, is lifted in the general dynamic heterogeneity scenario. The summation over t_{probe} gives rise to $D(\Gamma)$ under the implicit assumption that v_{probe} and t_{probe} are large enough to resolve the fluctuations and, for dispersive relaxation, that implicit averaging over V_{expt} (q-averaging) is accounted for. The non-Fermi-liquid phase is considered as a dense set of incoherent fluctuations (characterized by their relaxation rates, Γ_i) between which the system evolves. Here we explore the possibility through a discussion of the magnetization-density correlation function, $C(t)$. We define the following Fourier transform pair:

$$
\begin{aligned}
C(t) &= \int_{-\infty}^{\infty} \mathrm{d}\omega\, \mathrm{e}^{-\mathrm{i}\omega t} \chi(\omega) \\
\chi(\omega) &= \frac{1}{2\pi} \int_{-\infty}^{\infty} \mathrm{d}t\, \mathrm{e}^{\mathrm{i}\omega t} C(t).
\end{aligned}
\tag{A1.5}
$$

For notational convenience, any spatial dependence (i.e. limits imposed both by spatial size of heterogeneity and dispersion) is momentarily neglected, and, with the focus on the time evolution, the integral (A1.3) may be written as

$$
\chi(\omega) = \int \mathrm{d}\Gamma\, D(\Gamma)\chi(\Gamma;\omega) = \sum_i W(\Gamma_i)\chi(\Gamma_i;\omega)
\tag{A1.6}
$$

where $W(\Gamma_i) = W_i$ is the weight associated with relaxation rate Γ_i occurring within a primary field fluctuation of the temporal representation, $n_i \tau_i / T_{\mathrm{expt}}$ (cf. the volumetric representation $n_i v_i / V_{\mathrm{expt}}$). This gives the correlation function, $C(t)$:

$$
C(t) = \int_{-\infty}^{\infty} \mathrm{d}\omega\, \mathrm{e}^{-\mathrm{i}\omega t} \int \mathrm{d}\Gamma\, D(\Gamma)\chi(\Gamma;\omega) = \sum_i W_i C_i(t)
\tag{A1.7}
$$

with the contribution of the ith relaxation rate:

$$
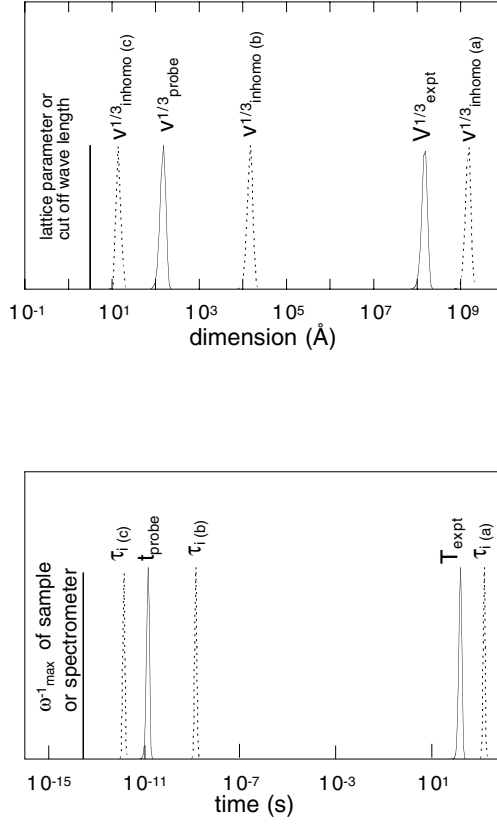C_i(t) = \sum_j \theta_{ji} g_{ij}(\tau_i; t)
\tag{A1.8}
$$

Figure A1. Upper frame: a typical distribution of spatial length scales in a neutron scattering problem appropriate to the row headings of table A1. Schematically similar diagrams apply for x-ray and quasiparticle scattering. In a given experiment, the spreads of v_{probe} and v_i may be significantly larger than indicated, leading to partial resolution of, for instance, the distribution of heterogeneities. The cases are as follows: (a) an effectively homogeneous sample; (b) a spatial incoherent sum of heterogeneities over V_{expt} is to be taken; (c) a coherent spatial sum of heterogeneities over v_{probe} is to be taken. The correlation length of the magnetic fluctuations must be considered in each case. Lower frame: a typical distribution of temporal length scales in a neutron scattering problem appropriate to the column headings of table A1. Schematically similar diagrams apply for x-ray and quasiparticle scattering. The cases are as follows: (a) static heterogeneities; (b) an incoherent temporal sum of heterogeneities over T_{expt} is to be taken; (c) a coherent temporal sum of dynamical heterogeneities over t_{probe} is to be taken. The overlap of the central distribution, $D(\Gamma)$, with the spread of both τ_i and t_{probe} must be considered in each case.

where, for an interval τ_i as in figure A2,

$$g_{ij}(\tau_i; t) = \frac{1}{\tau_i} \int_{-\tau_i/2}^{\tau_i/2} dt' \, m_i(t')m_j(t' + t) \tag{A1.9}$$

and θ_{ij} is the coherence function between intervals i and j. The characteristic time intervals, τ_i, may be regarded as time domains superposed on the inverse relaxation rate in analogy with volume domains (e.g. of moment direction) which exist on top of the spatial correlation length. In the Fermi liquid $\theta_{ij} = 1$ for all pairs i, j, whilst the incoherence characteristic of the non-Fermi-liquid reduces this to $\theta_{ij} = \delta_{ij}$. Parenthetically, it is noted that, from this perspective, SED may arise in two distinct ways. First, on tuning the degree of coupling in the

primary response function to the local environment via the temperature, doping, or pressure, etc, the distribution $D(\Gamma)$ may renormalize and become sufficiently narrow that differences in relaxation-rate renormalization become negligible, $(\Gamma_2 - \Gamma_1) \ll \sqrt{(\Gamma_1 \Gamma_2)}$, whilst τ_i remains less than T_{expt} giving a normal paramagnon (Fermi-liquid like) response; alternatively, the tuning may suppress local renormalization giving rise to $D(\Gamma) \sim \delta(\Gamma - \Gamma_0)$. Within a given context the meaning will be clear. In the case of incoherence, $\theta_{ij} = \delta_{ij}$, there are two possible regions of behaviour within each of the categories of table A1 corresponding to $\Gamma_i \tau_i$ being greater or less than unity. In the first, the correlation function is determined by $D(\Gamma)$ given that the contributions over each time interval τ are complete, such a non-Fermi-liquid state may be thought of as a multiple Fermi liquid which is independent of the distribution of τ. In contrast, when dominated by strong perturbations which distribute τ over small time intervals and break the condition $\Gamma \tau \geqslant 1$, a more careful discussion of the distribution of the phase coherence time $\mathcal{D}(\tau)$ in relation to $D(\Gamma)$ and t_{probe} is required (figure A1, lower frame). The former situation will prevail for a (self-consistent) response dominated by fluctuations in the primary variable and at least for the higher-frequency magnetic relaxation rates in the presence of secondary-field heterogeneities. The latter scenario is compatible with dynamical heterogeneities driven by a secondary field. In dealing with spatial heterogeneity, similar considerations apply for the correlation length, ζ, and the volume of heterogeneity.

The approximate constancy of u allows the renormalization in amplitude and relaxation rate of the dynamical susceptibility to be effected through χ_i^{-1}. Consequently the change in microscopic dynamics from one time interval, τ_i, to another may be marked by the value of χ_i^{-1}. The fluctuation-dissipation theorem relates a high susceptibility to enhanced magnetic correlations; a high-susceptibility state is therefore liable to be robust and have an extended lifetime, τ. In the light of this, the Curie–Weiss like temperature dependence of the lowest relaxation rate, Γ_1, observed at elevated temperature in UCu_4Pd may be rationalized through a heuristic appeal to the presence of persistent, residual, antiferromagnetic correlations.
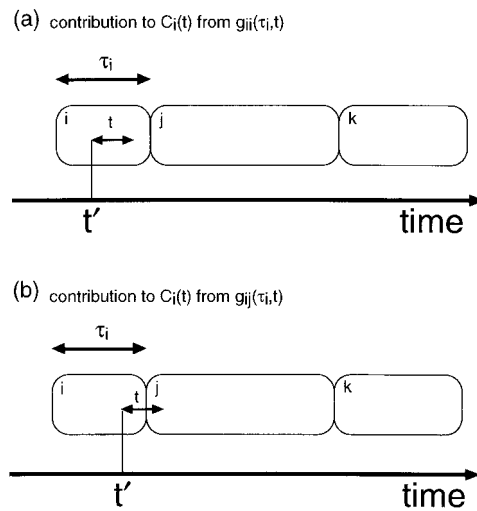
(a) contribution to $C_i(t)$ from $g_{ii}(\tau_i,t)$

(b) contribution to $C_i(t)$ from $g_{ij}(\tau_i,t)$

Figure A2. Schematic representations of heterogeneity time intervals, τ_i. In the upper part, (a), the correlation function is to be evaluated within a given time interval τ_i corresponding to a contribution $g_{ii}(\tau_i, t)$. In the lower part, (b), the cross term, $g_{ij}(\tau_i, t)$ is illustrated. On the assumption of incoherence in the non-Fermi-liquid phase, this cross term is neglected, whilst in the (coherent) Fermi-liquid state, it is to be included.

A1.4. Dynamic heterogeneity

Categories (1), (2), (4), (5) assume each microregion within V_{expt} to evolve independently. The presence of dynamic spatial inhomogeneity implies averaging over both V_{expt} and T_{expt} with the caveat that the restrictions concerning v_{probe} and t_{probe} are applied. The central inference of the analysis is the concept of a heterogeneity dependence of the relaxation rate, $\Gamma_X = \Gamma_0 f(X)$, in contrast with the SED scenario with one (wavevector dependent) relaxation rate, $\Gamma_0(q)$, applicable to the dissipation of all spontaneous fluctuations in the magnetization density. Results of sections 2 and 3 suggest the simplest form, $\Gamma_X = \Gamma_0(\chi_0/\chi_X)$, i.e. scaling of the relaxation rate with the local susceptibility, to capture the essential effects. Apart from magnetization-density fluctuations, the origin of the local renormalization of χ may include secondary fields—for example, spontaneous fluctuations in the atomic position and orbital occupation (e.g. valence, screening, and crystal-field fluctuations) or a conservation law, as in the exhaustion of screening.

Given that the (divergent) spin-density fluctuations themselves may act as regions of local susceptibility enhancement, a profound difference may be expected between the behaviour of materials with and without approximate spin conservation. In the former, creation or annihilation of a spontaneous spin-density fluctuation requires transport of the excess spin density over the length scale of the inhomogeneity (Γ is necessarily dispersive), whilst in the latter, creation or annihilation may take place on a local scale. The decoupling of the size of the fluctuation and the length scale over which relaxation occurs implies that, in systems without spin conservation, the local susceptibility enhancement will be effective for the full complement of modes. In contrast, spin-conserving systems have a tendency to narrow distributions, $D(\Gamma)$, at long wavelengths where the principal enhancements are anticipated. In the light of this, non-spin-conserving materials may be expected to exhibit the more pronounced signatures of extended distributions $D(\Gamma)$ and associated non-Fermi-liquid behaviour in the vicinity of critical points.

A1.5. Implicit incoherence of modes and the emergence of phase locking

The non-Fermi-liquid susceptibility has been expressed as an incoherent sum, equation (1.1); there is no inclusion of cross coupling terms [17, 45]. From the perspective of the dynamic, slow-mode model we have no contributions which span more than one interval of coherence time (τ), the absence being an expression of a basic phase incoherence in the non-Fermi-liquid state. The lack of phase coherence between τ-intervals precludes formation of a feedback field, the growth of a particular χ_i, and associated dominant-mode behaviour. In order to pass from the non-Fermi-liquid to coherent Fermi-liquid regimes, temperature, external fields, pressure, or chemical composition must be exploited to stabilize a dominant mode. The concomitant elimination of phase incoherence between dynamical heterogeneities over significant time intervals introduces a degree of rigidity into the dynamics which may permit growth of an oscillatory (damped) decay in the magnetization density and give rise, in a continuous fashion, to the evolution of spectral forms of χ'' characteristic of strongly correlated states. An example may exist in the transfer of spectral weight in the paramagnetic phases of the UCu_5–UCu_4Pd system where the low-energy mode, located around Q_{afm} in UCu_5, is replaced by a wavevector independent response broadly distributed in energy, entirely consistent with the increasing importance of phase-incoherent dynamical heterogeneities as suggested by the analysis of the inelastic neutron scattering and heat capacity data in section 3. That is, at a fundamental level, fluctuations have an amplitude and phase (ultimately derived from those of the underlying quantum field) both of which may depend on (r, t). The phase correlations

may, for instance, be spatially weak with long time duration as in the formation of microscopic domains and, in general, are characterized by a multiple space-time covariance function. For a given experiment, the measured quantity is strongly influenced by the ratio of the probe space-time coherence volume to the characteristic scales of this multivariate correlation function. In instances where the covariance decays rapidly, a short-timescale probe, e.g. resonant x-ray scattering, may be anticipated to give an enhanced response in comparison with a measure of the (quasi-) equilibrium response as revealed through, for example, C/T, NMR, or inelastic neutron scattering. As noted in the analyses of UCu_4Pd, section 3.1.5, and $CeCu_{5.9}Au_{0.1}$, section 3.2.3, the approach to magnetic order may, in some instances, involve the loss of high-frequency relaxation rates (figure 2(c)) followed by the softening of the lowest relaxation rate in the immediate vicinity of the transition. Such a perspective may shed some light on the problem of probe-dependent (nominal) critical points observed for example in weakly (antiferro-) magnetic heavy-fermion superconductors. Similar considerations are involved in the spatial domain (see [44] and references therein).

For heterogeneities where the probe space or time coherence volume is small on the scale of the inhomogeneity—categories (4), (5), (6) and (2), (5), (8) of table A1 respectively—the $\langle \ \rangle_{T_{\text{expt}}, V_{\text{expt}}}$ averaging of the correlation function over the independent probe coherence volumes is incoherent. In the opposite regime—categories (1), (3), spatial and (1), (7), temporal—the intrinsic incoherence of adjacent heterogeneities plays an essential role; microscopically, a (weak) localization of the phase eigenmode to a given heterogeneity may be invoked. Such localization is anticipated to be most effective in the presence of a wide segregation of limited volumes having well resolved eigenmodes. With the emergence of heterogeneous regions of successively larger τ_i and v_i, the energy spacing between eigenmodes decreases, the discrete nature (incoherence) of the dynamical heterogeneity is lost, and the system passes towards a coherent (Fermi-liquid) regime.

A1.6. C/T in the dynamical heterogeneity model

A one-to-one correspondence of relaxation rate with volume of heterogeneity allows the (magnetic) relaxational contribution to the heat capacity to be written as follows:

$$\lim_{T \to 0} \frac{C}{T} = \frac{\upsilon \pi k_B^2}{3} \sum_i \sum_q \frac{1}{\Gamma_i} n_i \tag{A1.10}$$

where n_i is the degeneracy of volumes v_i occurring in V_{expt}. The number of modes is proportional to the number of effective magnetic ions in v_i; hence, for wavevector independent relaxation rates,

$$\sum_q \to \eta v_i \tag{A1.11}$$

and

$$\lim_{T \to 0} \frac{C}{T} = \eta \frac{\upsilon \pi k_B^2}{3} \sum_i \frac{n_i v_i}{\Gamma_i} \tag{A1.12}$$

giving, over the total volume,

$$\lim_{T \to 0} \frac{1}{V_{\text{expt}}} \frac{C}{T} = \eta \frac{\upsilon \pi k_B^2}{3} \sum_i \frac{n_i v_i}{V_{\text{expt}}} \frac{1}{\Gamma_i}. \tag{A1.13}$$

The correspondence $\Gamma_{v_i} \leftrightarrow v_i$ gives

$$\sum_i \frac{n_i v_i}{V_{\text{expt}}} \frac{1}{\Gamma_i} = \int d\Gamma \ D(\Gamma) \frac{1}{\Gamma} \tag{A1.14}$$

for a normalized distribution $D(\Gamma)$ and hence equation (2.30) in the main text.

A1.7. Homogeneous static state

In addition to phenomenological models for $\chi(q, \omega)$ which break with the underlying Fermiology [8], an alternative microscopic basis for a model $D(\Gamma)$ may be invoked via a starting set of non-interacting relaxation modes which propagate in a dispersive and non-linear medium. In the case of a set of normal modes with weak interactions, the resonance conditions of scattering, $\omega(q_1) + \omega(q_2) = \omega(q_3)$ and $\boldsymbol{q}_1 + \boldsymbol{q}_2 = \boldsymbol{q}_3$, must be satisfied at each collision; however, the presence of strong interactions broadens the modes and the conditions become less stringent. For overdamped modes the conditions may become sufficiently relaxed that any given $\Gamma(q)$ will interact with a host of other modes to generate a broad distribution at each wavevector. The multiple scattering of each starting mode will rapidly destroy the mutual phase correlations of a given scattering triad and may establish the incoherence embodied in equation (1.1). Viewed from an alternative perspective, anharmonicity is incompatible with wavevector/frequency eigenstates and implies space-time localization, i.e. formation of dynamical heterogeneities.

Appendix 2. *q*-space averaging

A2.1. Q-resolution in type 1 non-Fermi liquid

We start by assuming, for simplicity, that the intrinsic response is that of the SED:

$$\chi'' = \frac{\omega \Gamma \chi}{\omega^2 + \Gamma^2}. \tag{A2.1}$$

That is to say, there is a single relaxation rate, Γ, at each wavevector and temperature. No distribution of relaxation rates is invoked. What is measured (given our assumption of good energy resolution and loose q-resolution) is

$$\int \chi''(q, \omega)\, \mathrm{d}^d q = \int \frac{\omega \Gamma \chi}{\omega^2 + \Gamma^2}\, \mathrm{d}^d q \tag{A2.2}$$

where d is the dimension of q-space integration performed in the experimental realization of $\chi''(\omega)$. Writing $\mathrm{d}^d q$ as $g q^{d-1}\, \mathrm{d}q$ where g is a geometric factor of integration,

$$\int \chi''(q, \omega)\, \mathrm{d}^d q = \int \left[\frac{\Gamma(q) \chi(q) g q^{d-1}}{\mathrm{d}\Gamma/\mathrm{d}q} \right] \mathrm{d}\theta \tag{A2.3}$$

with

$$\Gamma(q) = \omega \tan(\theta). \tag{A2.4}$$

Setting the condition,

$$\frac{\Gamma(q) \chi(q) g q^{d-1}}{\mathrm{d}\Gamma/\mathrm{d}q} = \text{constant} = \frac{1}{B} \tag{A2.5}$$

one measures the following quantity:

$$\int \chi''(q, \omega)\, \mathrm{d}^d q = \int \frac{\mathrm{d}\theta}{B} = \frac{1}{B} \left[\arctan\left(\frac{\omega}{\Gamma(Q_1)} \right) - \arctan\left(\frac{\omega}{\Gamma(Q_2)} \right) \right]. \tag{A2.6}$$

This condition may be conveniently expressed as follows:

$$\Gamma(Q_2) = \Gamma(Q_1) \exp\left(B \int_{Q_1}^{Q_2} \chi(q)\, \mathrm{d}^d q \right). \tag{A2.7}$$

A2.2. 2d q-space averaging

In the case of a 2d integral and when $\chi(q)$ may be expressed in standard form we obtain

$$\Gamma(Q_2) = \Gamma(Q_1)\left[\frac{1 + \lambda^2 Q_2^2}{1 + \lambda^2 Q_1^2}\right]^{gB/(2c)} \tag{A2.8}$$

where the correlation length λ has been introduced in standard fashion, $\lambda^2 = c\chi$. If the integration is performed around the critical wavevector, i.e. $Q_1 = 0$, outwards, then

$$\Gamma(Q) = \Gamma(0)(1 + \lambda^2 Q^2)^{gB/(2c)} \approx \Gamma(0)\left(1 + \frac{gB}{2c}\lambda^2 Q^2\right). \tag{A2.9}$$

In the standard model for the relaxation rate, we obtain $\Gamma(Q) = \Gamma(0)(1 + \lambda^2 Q^2)$, since $1/B = g/(2c)$, giving

$$\langle \chi'' \rangle_{2D} = \frac{\pi}{c}\left[\arctan\left(\frac{\omega}{\Gamma(0)}\right) - \arctan\left(\frac{\omega}{\Gamma(0)(1 + \lambda^2 Q^2)}\right)\right]. \tag{A2.10}$$

A2.3. 1d q-space averaging

The $\chi'' = A[\arctan(\omega/\Gamma_1) - \arctan(\omega/\Gamma_2)]$ form is obtained in the case of a 1d q-space integration of equation (A2.1) given

$$\chi^{-1}(q) = \chi^{-1} + c_z q_z^2 \tag{A2.11}$$

and the condition

$$\Gamma(Q_{2z}) = \Gamma(Q_{1z})\exp\left(\frac{B\lambda_z}{c_z}\left[\arctan(\lambda Q_{2z}) - \arctan(\lambda Q_{1z})\right]\right). \tag{A2.12}$$

When working around the magnetic wavevector, i.e. $Q_{1z} = 0$, we have

$$\Gamma(Q_z) = \Gamma(0)\exp\left(\frac{B\lambda_z}{c_z}\left[\arctan(\lambda Q_z)\right]\right) \tag{A2.13}$$

which for *small* $\lambda_z Q_z$ gives

$$\Gamma(Q_z) = \Gamma(0)e^{B\chi Q_z} \tag{A2.14}$$

and for *large* $\lambda_z Q_z$ gives

$$\Gamma(Q_z) = \Gamma(0)e^{B\lambda_z \pi/(2c_z)}. \tag{A2.15}$$

Thus for materials where λ_z^{-1} is small, and lies within the spectrometer resolution, the relaxation rate may appear largely independent of Q_z, suggestive of local dynamics in this direction despite the strong correlations implied by a large correlation length λ_z.

For short correlation lengths we use the small-$\lambda_z Q_z$-expansion:

$$\Gamma(Q_z) = \Gamma(0)(1 + B\chi Q_z + \cdots). \tag{A2.16}$$

This is in some sense the opposite limit to that of the cuprate problem (where integration up to a large Q is performed) and results in a novel temperature dependence for Γ_2. Remaining close to the critical wavevector in the scattering plane and for small excursions, ΔQ_z, out of the plane we have $\Gamma(0) = u\chi^{-1} = uC^{-1}k_B(T - T_0)$ and hence

$$\Gamma(\Delta Q_z) = \Gamma(0) + Bu\,\Delta Q_z. \tag{A2.17}$$

Appendix 3. Limiting forms and extensions of $\chi(q, \omega)$

A3.1. Limits and approximate analytical forms for $\chi(q, \omega)$

The high-frequency expansion of the susceptibility is, for $\omega > \Gamma_1, \Gamma_2$,

$$\chi'' = \frac{u}{\omega}\left[1 - \frac{\Gamma_1^2 + \Gamma_2^2 + \Gamma_1\Gamma_2}{3\omega^2} + \cdots\right] \tag{A3.1}$$

whilst for low frequencies, $\omega < \Gamma_1, \Gamma_2$,

$$\chi'' = \frac{u\omega}{\Gamma_1\Gamma_2}\left[1 - \frac{\omega^2(\Gamma_1^2 + \Gamma_2^2 + \Gamma_1\Gamma_2)}{3\Gamma_1^2\Gamma_2^2} + \cdots\right]. \tag{A3.2}$$

It is instructive to plot $\log(\chi'')$ against $\log(\omega)$. In the high-temperature limit we take $\Gamma_1 \approx \Gamma_2 = ak_B(T - T_0)$ giving the high-frequency ($\omega > \Gamma$) approximation at high temperature as

$$\ln(\chi'') = -\ln\left(\frac{\omega}{u}\right) - \left(\frac{ak_B(T - T_0)}{\omega}\right)^2 + \cdots \tag{A3.3}$$

with a turning point at

$$\omega_{\text{high}} = \sqrt{2}ak_B(T + T_0) \tag{A3.4}$$

and the low-frequency ($\omega < \Gamma$) approximation at high temperature as

$$\ln(\chi'') = 2\ln\left(\frac{u}{ak_B(T - T_0)}\right) + \ln\left(\frac{\omega}{u}\right) - \left(\frac{\omega}{ak_B(T - T_0)}\right)^2 + \cdots \tag{A3.5}$$

with a turning point at

$$\omega_{\text{low}} = \frac{ak_B(T - T_0)}{\sqrt{2}}. \tag{A3.6}$$

In figure A3 the plot contains two dashed lines of plus and minus unity slope representing the first-order approximations to χ'', and two approximately parabolic curves which give the corrections to lowest order, equations (A3.1), (A3.2). The filled/open circles represent experimental data for UCu$_4$Pd at 300 K and 12 K respectively.

At intermediate frequencies, $\Gamma_1 \ll \omega \ll \Gamma_2$, χ'' saturates as

$$\ln(\chi'') = \ln\left(\frac{\pi u}{2\Gamma_2}\right) - \frac{2\omega}{\pi\Gamma_2}\left(1 - \left(\frac{\omega}{\Gamma_2}\right)^2\right) + \cdots \tag{A3.7}$$

giving rise to a $(1/f)$ noise band for magnetic fluctuations in the classical limit:

$$\langle m_\omega^2 \rangle \propto k_B T \frac{\chi''(\omega)}{\omega} \propto \left(\frac{k_B T u}{4\Gamma_2}\right)\frac{1}{f}. \tag{A3.8}$$

As $\Gamma_1 \to 0$, for example in the $q \to 0$ limit of spin-conserving systems, this may yield an alternative approach to the interpretation of macroscopic magnetic noise experiments where the essential role of dynamical heterogeneities yields a broad spectral response.

At the level of current neutron scattering experiments, the saturation at intermediate frequency, equation (A3.7), is seen in UCu$_4$Pd at low temperatures (figure A3, open circles), in good agreement with the value predicted from high temperatures. However, the data do not extend low enough in frequency to show the eventual low-frequency return to linear behaviour at 12 K.
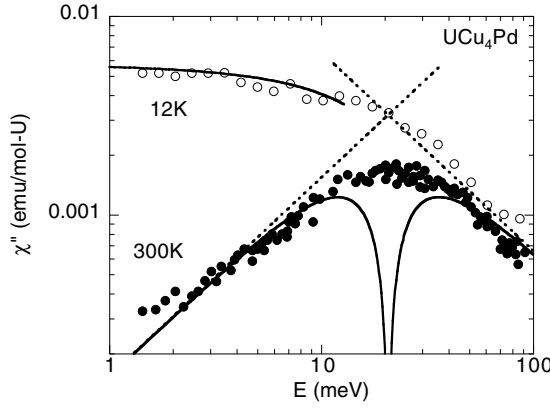
Figure A3. High-temperature data for UCu$_4$Pd (filled circles, 300 K) and low-temperature data (open circles, 12 K) are compared with the three limiting equations (A3.1), (A3.2), and (A3.7) (solid lines) for the frequency dependence of $\chi''(\omega)$. At 300 K, close to the paramagnetic regime, $\Gamma_1 \sim \Gamma_2$, both high- and low-frequency asymptotic limits are reached, enabling good definition of the three model parameters, u, Γ_1, Γ_2. (The dashed lines of plus and minus unity slope represent the first-order approximations to $\chi''(\omega)$ and the two approximately parabolic curves give the lowest-order corrections.) In contrast, the data at 12 K, whilst asymptotically approaching the saturation limit predicted from the high-temperature data, equation (A3.7), do not extend low enough in energy to enable a reliable estimate of $\Gamma_1(12\,\text{K})$ to be made. Using the data at saturation to estimate the mode frequency, $\sqrt{(\Gamma_1\Gamma_2)}$, yields $\Gamma_1 \sim 0.1 \pm 0.1$ meV at 12 K.

A3.2. General forms

A sometimes useful general form is

$$\chi(\omega) = \langle\chi\rangle \frac{\langle\Gamma\rangle}{\Gamma_2 - \Gamma_1} \ln\left[\frac{\Gamma_2 - i\omega}{\Gamma_1 - i\omega}\right] \tag{A3.9}$$

which permits one to extract a mean susceptibility, $\langle\chi\rangle$, under a given parametrization of $\langle\Gamma\rangle$; for example, using the mode frequency of $\chi''(\omega)$ as an estimator for $\langle\Gamma\rangle$ yields

$$\chi(\omega) = \langle\chi\rangle \frac{\sqrt{\Gamma_1\Gamma_2}}{\Gamma_2 - \Gamma_1} \ln\left[\frac{\Gamma_2 - i\omega}{\Gamma_1 - i\omega}\right]. \tag{A3.10}$$

When u is sensibly constant the expressions may simplify on expressing $\Gamma_{1,2}$ in terms of the inverse susceptibility, for example:

$$\chi'(q) = \frac{1}{\chi_2^{-1} - \chi_1^{-1}} \ln\left[\frac{\chi_2^{-1}}{\chi_1^{-1}}\right]. \tag{A3.11}$$

A3.3. Extension of the model beyond relaxational dynamics

Pursing the notion of the build-up of phase locking and the emergence of an oscillatory mode discussed in section A1.5 of appendix 1, a natural progression away from purely relaxational dynamics is to consider the spectrum of a set of phase-incoherent oscillators of frequency Δ under a distribution of relaxation rates $D(\Gamma)$. By extension of equation (2.1), the susceptibility for a damped oscillator may be written as

$$\chi^{-1}(q,\omega) = \chi^{-1}\left[1 - \frac{\omega^2}{\Delta^2} - \frac{i\omega}{\Gamma}\right] \tag{A3.12}$$

which gives, on integration over the inverse susceptibility,

$$\chi'' = \frac{u}{\Gamma_2(\omega) - \Gamma_1(\omega)} \left[\arctan\left\{ \frac{\omega}{\Gamma_1(\omega)} \right\} - \arctan\left\{ \frac{\omega}{\Gamma_2(\omega)} \right\} \right] \tag{A3.13}$$

where

$$\Gamma_{1,2}(\omega) = \Gamma_{1,2}\left[1 - \omega^2/\Delta^2 \right]. \tag{A3.14}$$

At low frequencies, for $\omega \ll \Delta$ we recover equation (2.4):

$$\chi'' = \frac{u}{\Gamma_2 - \Gamma_1} \left[\arctan\left(\frac{\omega}{\Gamma_1} \right) - \arctan\left(\frac{\omega}{\Gamma_2} \right) \right] \tag{A3.15}$$

giving, as $\omega \to 0$, an initial linear rise:

$$\chi'' \to \frac{u\omega}{\Gamma_1 \Gamma_2}. \tag{A3.16}$$

In the vicinity of the pole, $\omega \sim \Delta$, one has

$$\chi'' = \frac{u}{\omega} \left[1 - \frac{(\Gamma_1^2(\omega) + \Gamma_2^2(\omega) + \Gamma_1(\omega)\Gamma_2(\omega))}{3\omega^2} + \cdots \right]. \tag{A3.17}$$

For $\omega = \Delta + \delta$, this gives

$$\chi'' = \frac{u}{\Delta} \left[1 - \frac{\delta}{\Delta} + O\left(\frac{\delta}{\Delta} \right)^2 + \cdots \right] \tag{A3.18}$$

which is to first order independent of Γ_1, Γ_2 and yields the peak of χ'' *below* the resonant frequency. Finally, for $\omega \gg \Delta$,

$$\chi'' \to \frac{u\Delta^4}{\omega^3 \Gamma_1 \Gamma_2} \tag{A3.19}$$

giving a rapid fall-off at high frequencies. The full form, with the characteristic linear rise, broad peak with its maximum displaced to energies below the pole, Δ, and rapid decay at high frequency is portrayed for some parameter values typical of the high-T_c YBa$_2$Cu$_3$O$_{7-\delta}$ system in the underdoped regime in figure A4.

To give a simple description of the changes in the scattering cross section above and below the superconducting phase transition, we consider, within the dynamical heterogeneity paradigm, the evolution with cooling from high temperatures for slightly underdoped cuprates. Starting above the pseudogap temperature, T^*, where the fluctuations are mutually incoherent, cooling brings the system into the pseudogap regime, $T^* > T > T_{sc}$, with a build-up of phase coherence between the magnetic heterogeneities. This is followed by condensation of the superconducting phase, $T_{sc} > T > 0$. Evidence for mode softening and non-Fermi-liquid q-selection below T^* in the vicinity of the antiferromagnetic wavevector, $Q_0 = (\pi/a, \pi/a)$, in the pseudogap region comes directly from (i) the predominant weight of the neutron scattering cross section at Q_0 and (ii) the observation that on approaching the antiferromagnetic composition (i.e. increasing strength of Q_0-correlations), T^* increases. Passing below T_{sc}, the total intensity in neutron energy-loss scattering in the vicinity of the resonance energy is given by an essentially unchanging non-Fermi-liquid like contribution (the pole of χ'' as given in equation (A3.17) is independent of changes in damping rate Γ_1, Γ_2 driven by the condensation of the superconducting state), in addition to a contribution arising from the destruction of Cooper pairs[12]. Given their different physical origins, the former being a generalization of the

[12] In the Fermi liquid the quasiparticle states concentrated around ε_{Fermi} disappear for $T \ll T_{sc}$. In a non-Fermi liquid where the quasiparticle resonance is poorly defined in (q, ω) space, the reduction of spectral weight may, in general, be less dramatic.
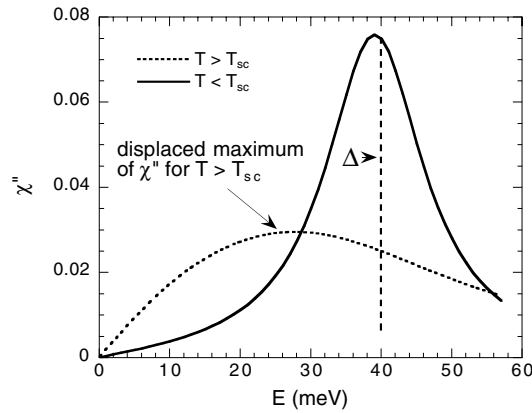
Figure A4. An example of the form of equation (A3.15) for the response of a set of phase-incoherent oscillators of fixed pole having a distribution of relaxation rates. The dashed line has parametric values of the pole frequency $\Delta = 40$ meV with lower and upper limits on the relaxation rate of 15 and 35 meV. Characteristically, the normal-state response is a broad distribution with an initial approximately linear rise and a maximum of χ'' strongly displaced from Δ. The solid line is the spectrum maintaining the same pole with increased damping and amplitude multiplied by a factor of three. As discussed in the text, these plots may be crude representations of the response of lightly underdoped high-T_c materials on passing through the superconducting phase transition.

normal magnetic particle–hole correlation whilst the latter arises from annihilation of coherent particle–particle correlations, the energy and q-widths of these two contributions may differ. As regards the part arising from scattering by an ensemble of phase-coherent Cooper pairs, the neutron cross section may be broadly split into two parts: (i) the product of a factor expressing the indistinguishable nature of transitions from the superconducting state and the density of final states which largely governs the intensity (i.e. this factor only arises in the presence of superconducting phase coherence even if its amplitude depends on the Cooper pairing symmetry and binding energy and it drops to zero with the superconducting phase coherence at T_{sc}) and (ii) a resonant denominator which reflects the pair binding energy. In high-T_c superconductors, one may see the separation of the two effects as the sharp contrast between (i) the rise in scattering intensity as superconducting phase coherence develops on cooling below T_{sc} and (ii) the stability of the pole position, E_{res} [46]. The structure of the Fermi surface in conjunction with strong evidence for a phase change of π of the symmetry of the superconducting order parameter at Q_0 suggests the presence of a superconducting phase coherence weighting factor of 2 in the cross section relative to the normal state contribution for $T \ll T_{sc}$ [47]. Thus in the underdoped regime around (Q_0, E_{res}) the $\sim$3-fold change in cross section for $T \ll T_{sc}$ to $T > T_{sc}$ [46] may be rationalized in terms of one (essentially unchanged) unit from the non-Fermi-liquid pole in addition to $\sim$2 units (superconducting coherence factor) from the annihilation of Cooper pairs. In figure A4, for $T < T_{sc}$ the total susceptibility has been approximated as three times that calculated in the non-Fermi-liquid phase with the suppression of slow relaxation processes simulated by setting the relaxation rates, Γ_1, Γ_2, to numerically larger values[13]. For a small shift in chemical doping to optimal T_{sc} where the values of T^* and T_{sc} approximately coincide, the neutron scattering amplitude at (Q_0, E_{res}) gives the cleanest signature of the superconducting phase transition with a fall to the

---

[13] From equations (4.6), (4.7) it is clear that such changes in Γ_1, Γ_2 will force the response for $\omega < \Delta$ and $\omega > \Delta$ to fall, simultaneously shifting the peak response to the pole and making it relatively pronounced whilst not affecting its amplitude.

nominal background intensity for $T > T_{sc}$ as the system dissolves into local, phase-incoherent fluctuations of essentially zero relative amplitude above $T_{sc} \sim T^*$.

References

[1] Demuer A *et al* 2000 *J. Low Temp. Phys.* **120** 314
[2] Salce B *et al* 2000 *Rev. Sci. Instrum.* **7** 2461
[3] Debenedetti P G and Stillinger F H 2001 *Nature* **410** 259
[4] Chamberlin R V and Kingsbury D W 1994 *J. Non-Cryst. Solids* **172–174** 318
[5] Chamberlin R V 1999 *Phys. Rev. Lett.* **82** 2520
[6] Chamberlin R V 1996 *Europhys. Lett.* **33** 545
[7] Chamberlin R V 2000 *Nature* **408** 337
[8] Varma C M *et al* 1989 *Phys. Rev. Lett.* **63** 1996
[9] Hayden S M *et al* 1991 *Phys. Rev. Lett.* **66** 821
[10] Keimer B *et al* 1991 *Phys. Rev. Lett.* **67** 1930
[11] Hayden S M *et al* 1992 *Phys. Rev. Lett.* **68** 1061
[12] Miranda E *et al* 1996 *J. Phys.: Condens. Matter* **8** 9871
[13] Aronson M C *et al* 1996 *J. Phys.: Condens. Matter* **8** 9815
[14] Bernhoeft N *et al* 1989 *Phys. Rev. Lett.* **62** 657
[15] Bernhoeft N *et al* 1986 *Physica* B **136** 443
[16] Hayden S M *et al* 2000 *Phys. Rev. Lett.* **84** 999
[17] Bernhoeft N *et al* 1998 *Phys. Rev. Lett.* **81** 4244
[18] Coad S *et al* 2000 *Physica* B **281** 200
[19] Bao W *et al* 1998 *Phys. Rev.* B **58** 12 727
[20] Cox D L *et al* 1985 *J. Appl. Phys.* **57** 3166
[21] Loidl A *et al* 1992 *Phys. Rev.* B **46** 9341
[22] Walter U *et al* 1986 *Z. Phys.* B **62** 325
[23] Braithwaite D *et al* 2000 *J. Phys.: Condens. Matter* **12** 1349
[24] Raymond S *et al* 1997 *J. Low Temp. Phys.* **109** 205
[25] Schröder A *et al* 1998 *Phys. Rev. Lett.* **80** 5623
[26] Hill T L 1994 *Thermodynamics of Small Systems* (New York: Dover) (reprint)
[27] Sachdev S 2000 *Science* **288** 475
[28] Edwards D and Lonzarich G G 1992 *Phil. Mag.* B **65** 1185
[29] Lonzarich G G 1986 *J. Magn. Magn. Mater.* **54** 612
[30] Pippard A B 1987 *Eur. J. Phys.* **8** 55
[31] Aronson M C *et al* 1995 *Phys. Rev. Lett.* **75** 725
[32] Aronson M C *et al* 1997 *Europhys. Lett.* **40** 245
[33] Bernal O O *et al* 1995 *Phys. Rev. Lett.* **75** 2023
[34] Vollmer R *et al* 1997 *Physica* B **230** 603
[35] Büttgen N *et al* 2000 *Phys. Rev.* B **62** 11 545
[36] Walter U *et al* 1987 *Phys. Rev.* B **36** 1981
[37] Bernhoeft N 2001 *J. Phys. Soc. Japan Suppl.* A **70** 7
[38] Tsujii H *et al* 2000 *Phys. Rev. Lett.* **84** 5407
[39] Stockert O *et al* 1998 *Phys. Rev. Lett.* **80** 5627
[40] Schröder A *et al* 2000 *Nature* **407** 351
[41] von Löhneysen H *et al* 2000 *J. Alloys Compounds* **303–304** 480
[42] Imai T *et al* 1993 *Phys. Rev. Lett.* **70** 1002
[43] Murata K K and Doniach S 1972 *Phys. Rev. Lett.* **29** 285
[44] Bernhoeft N 1999 *Acta Crystallogr.* A **55** 274
[45] Bernhoeft N and Lonzarich G G 1995 *J. Phys.: Condens. Matter* **7** 7325
[46] Bourges P *et al* 2000 *Science* **288** 1234 and references therein
[47] Bernhoeft N 2000 *Eur. Phys. J.* B **13** 685